

Anonymous Referee #1

The manuscript describes CR-SIM, a radar and multi-instrument emulator that has a wide range of potential applications. CR-SIM is freely available to the scientific community and has the interfaces necessary to be broadly used (e.g., compatibility with major community models, physics schemes and data formats). Thus, this is an impactful study and provides an important overview of the tool and its applications.

The manuscript layout is excellent and easy to follow. Overall, the methods employed are sound and the analyses are well described. The only major comment I have is that the description of the radar emulator needs more specific details as described below. I also have some other minor and technical comments to consider.

Thank you very much for your comments and suggestions. Providing this valuable feedback has helped to improve the current manuscript. We have modified the manuscript, taking into account the referee's comments. The following contains our detailed responses to referee's comments, with our responses in plain type given underneath your original comments in bold type.

General comments:

1) Since the goal of this journal is to make the model reproducible, more equations, references, and is needed for the following items to achieve this:

a. How are the model PSDs transformed into radar variables? The authors acknowledge Dr. Vivekanandan's the Mueller Matrix code at the end, but I didn't see this cited or described in the text.

The radar observables are computed by integrating scattering properties over the discrete PSD using a constant size bin for each hydrometeor. The complex scattering amplitudes for equally spaced particle sizes are pre-computed and stored in the look-up tables using the Mishchenko's T-matrix code for single non-spherical particles at a fixed orientation. Using the calculated scattering amplitudes, we computed radar observables following Ryzhkov et al. (2011), accounting for an assumption of the orientation distribution which can be selected by the user. We described the information in section 2 in the revised manuscript. Because the equations of radar observables have been well described in Ryzhkov et al. (2011) and are not unique to CR-SIM, we decided to not add them in the manuscript. The method is fully described in the Section 4.4 and 4.5 in the CR-SIM User Guide (<ftp://ftp.radar.bnl.gov/outgoing/moue/crsim/docs/crsim-UserGuide-v3.3.0.pdf>).

To verify our computations of radar variables, we employed Dr. Vivekanandan's Mueller-matrix-based code from Vivekanandan et al. (1991). The figure below shows an example of a comparison of radar reflectivity for raindrops computed using the methods in CR-SIM and the Mueller-matrix-based code. The results show consistent values. Figures 4 and 5 in the CR-SIM User Guide compare all radar variables at 3 GHz and 9.5 GHz for raindrops. We revised the acknowledgement section to state how the Mueller-matrix-based code was used.

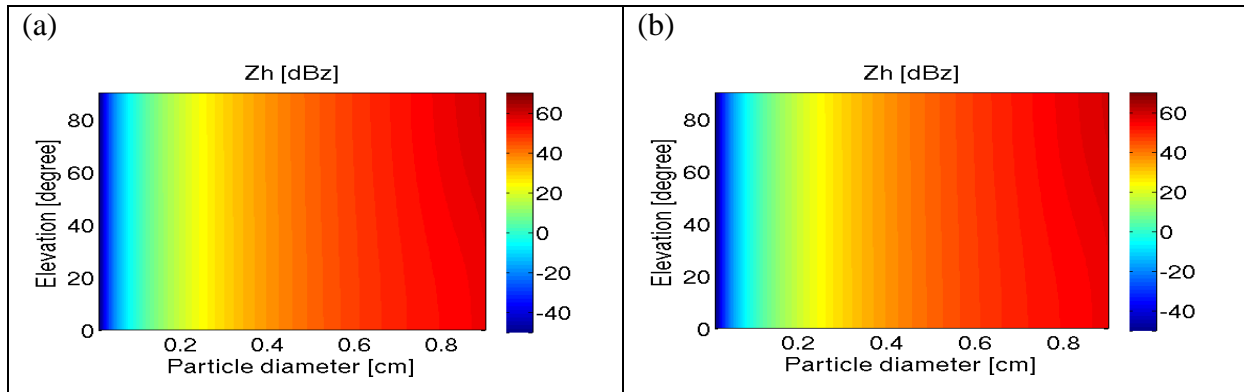


Figure: Comparison of Radar reflectivity at 3 GHz for raindrops as a function of elevation and particle size (diameter of an equi-volume sphere) computed by (a) method used in the CR-SIM based on Mishchenko's T-matrix code for a non-spherical particle at a fixed orientation and Ryzhkov's formulas for angular moments, and (b) the Mueller-matrix-based code from Vivekanandan et al. (1991).

b. How is the radar antenna pattern and pulse emulated? What are the range and antenna weighting patterns and are there different options?

We did not emulate the radar antenna pattern in CR-SIM. In the post-processing instrument model to convert grid data into radar polar coordinate data, we simply use a Gaussian function as a radar directivity function and average simulated radar observables within a range-gate bin with the gaussian weighting in the beam angle and range directions. We added the information to Section 2.3.

c. How are mixed phase hydrometeors treated in the calculation of scattering amplitudes, and how are the mixing ratios of these particles computed from pure liquid and pure ice hydrometeor classes in the models?

CR-SIM treats hydrometer categories for which mixing ratio (and/or number density) were predicted in the input cloud model using the selected microphysics scheme. At this stage, all ice hydrometeors (e.g., snow, ice, graupel, hail) are modeled as dielectrically dry spheroids i.e., assuming the dry growth of larger ice particles. Thus, the refractive index of dielectrically dry hydrometeors depends on relative mixture of air and solid ice. In other words, the refractive index depends on hydrometeor density and is computed using Maxwell Garnett (1904) mixing formula.

2) To give readers a sense of the computational requirements and burden for running a simulation, can you please describe what computing platforms were used for these simulations and what the simulation run times are?

We used a computer having 500-GB memory and 24 processors (Intel(R) Xeon(R) CPU E5-2670 v3 @ 2.30GHz) with 12 cores each for the simulations presented in the manuscript. The runtime depends on how many threads are used, simulation domain size, and the numbers of cloudy

gridboxes. The following is an example of computer resources and runtime for the simulation of the MCS case in Fig. 1.

Domain size: 667 x 667 x 12

Number of threads used: 16

Runtime: 270 sec

Specific Comments:

Lines 73 – 87: A little deeper treatment of past radar simulators and where the authors' contribution fits is warranted. For example, aside from the applications, this will enable the reader to more clearly see what the strengths and weaknesses of the radar emulator are and how they compare to other emulator tools. For example, some radar emulators such as Snyder et al. (2017a,b) apply a radar forward simulator to the model grid cells whereas other simulators account for the radar observing geometry (e.g., beamwidth, range resolution). Other simulators emulate radar time series signals based on model turbulence whereas others do not. Finally, some simulators take into account complex electromagnetics of hydrometeors or other weather radar observed scatterers.

C. Capsoni, M. D'Amico, and R. Nebuloni, 2001: A multiparameter polarimetric radar simulator. *J. Atmos. Ocean. Technol.*, 18, 1799–1809.

Caumont, O., V. Ducrocq, G. Delrieu, M. Gosset, J. Pinty, J. Parent du Châtelet, H. Andrieu, Y. Lemaître, and G. Scialom, 2006: A Radar Simulator for High-Resolution Nonhydrostatic Models. *J. Atmos. Oceanic Technol.*, 23, 1049–1067, <https://doi.org/10.1175/JTECH1905.1>.

B. L. Cheong, R. D. Palmer, and M. Xue, 2008: A time series weather radar simulator based on high-resolution atmospheric models. *J. Atmos. Ocean. Technol.*, 25, 230–243.

Jiang, Z., M.R. Kumjian, R.S. Schrom, I. Giammanco, T. Brown-Giammanco, H. Estes, R. Maiden, and A.J. Heymsfield, 2019: Comparisons of Electromagnetic Scattering Properties of Real Hailstones and Spheroids. *J. Appl. Meteor. Climatol.*, 58, 93–112, <https://doi.org/10.1175/JAMC-D-17-0344.1>.

One of the features of using CR-SIM is it produces both radar and lidar observables for all the cloud resolving model grid boxes accounting for elevation angles relative to a radar location, similar to Snyder et al. (2017a,b), rather than other radar simulators that account for radar geometry characteristics such as beamwidth and radar range resolution to simulate scatters within the radar resolution volume (e.g., Capsoni et al, 2001; Caumont et al., 2006; Cheong et al., 2008). The radar sampling characteristics are accounted for in the post processing instrument model, as explained in the response to the referee's comment #1b. This feature facilitates the process of configuring any desirable observational setup with a varying number of profiling or scanning sensors.

The LUTs of scattering properties incorporated in the current CR-SIM were created using the T-matrix method where solid phase hydrometeors are represented as dielectrically dry oblate spheroids. These assumptions are rather simple compared to some other radar simulators which take into account complex electromagnetic scattering by mixed-phase hydrometeors or ice hydrometeors with possibly irregular shapes (e.g., Snyder et al., 2017a,b; Jiang et al., 2019). However, such complex electromagnetic scatters can be easily incorporated by adding LUTs of their scattering properties from different scattering calculation methods. In CR-SIM, a “scattering

type” refers to each hydrometeor class for which the look-up tables were pre-built for a set of assumptions. Every hydrometeor specie present in the cloud model output must be assigned to the corresponding scattering type in the CR-SIM configuration setting. This approach enables addition of the new “scattering types” obtained using different and more complex scattering assumptions (e.g., Kneifel et al., 2017; Leinonen and Moisseev, 2015; Leinonen and Szyrmer, 2015; Lu et al., 2016) without any change to the code.

We added these descriptions in summary and section 2. Thank you for the suggestions and pointing out those papers.

Line 90: and spectrum width?

Yes. We added spectrum width to the sentence.

Line 105: What particle size spacing is used and what are the minimal and maximum sizes of particles simulated? The truncation can affect the resulting simulated measurements.

We set the minimum and maximum sizes and size spacing of simulated particles for each hydrometeor category within the bulk microphysics schemes, except for the P3 scheme. ‘Particle size’ here refers to the particle maximum dimension. We added the information to the revised manuscript.

Category	Minimum size [μm]	Maximum size [μm]	Size spacing [μm]
Cloud	1	250	1
Drizzle	1	250	1
Rain	100	9000	20
Ice	1	1496	5
Snow, aggregates	100	50000	100
Graupel	5	50005	100
Hail	5	50005	100

Lines 105 – 114: In general, I could follow the authors’ description of the scattering properties and implement it into a simulator. However, there is no description of how mixed phase hydrometeors are treated. How is this accomplished?

Please see our response to the referee’s comment 1c.

Line 197: Suggest “for convective cells” since multiple convective cells are evident in the image

Done.

Line 251: Should add a reference for the Morrison microphysics scheme

Done. We added Morrison et al. (2005).

Line 282: It isn't clear which simulation output is saved every 10 minutes (CR-SIM or WRF LES), or both.

The WRF LES output is saved every 10 minutes, and CR-SIM is run for each output file. We revised the sentence.

Lines 289 – 290: Is spatial or temporal sampling driving these major errors?

We think that both can be major sources of the errors. We revised the sentence to read “the limited spatial and/or temporal sampling is the major error source to consider when comparing the profiling measurement derived CFP with the domain-averaged WRF CFP.”

Line 332: Should this say minimum detectable reflectivity Z_{min} , similar to a KASCR? Can you please provide the sensitivity of the simulated radar?

The minimum detectable reflectivity Z_{MIN} in the simulation is given by Eq. (4) with a constant $C=-50$ dBZ, which is similar to the Ka-band ARM scanning cloud radar (KaSACR). We revised the sentence.

Lines 342 – 343: How does this compare to the current CWRHI measurement interval?

The CFP estimation technique was applied to the Ka-band ARM scanning cloud radar at SGP. The product is available from the ARM Archive as an evaluation stage (<https://iop.archive.arm.gov/arm-iop-file/0eval-data/wang/kasacradv3d3c/README.html>). The CWRHI scans used in the product were provided at 20 sec intervals, which is a higher temporal resolution than that assumed in this study.

Lines 351 – 352: References needed for multi-Doppler error sources

We referred to Clark et al. (1980), Bousquet et al. (2008), and Potvin et al. (2012) in the revised manuscript.

Line 356: Which advection-correction technique? Please state and cite

Oue et al. (2019) used the advection-correction technique proposed by Shapiro et al. (2010) that allows for trajectories of multiple individual clouds, performs smooth grid-box-by-grid-box corrections of cloud locations, and takes into account changes in cloud shape with time by using PPI scans at two times. We added this description and reference to the revised manuscript.

Lines 364 – 366: While this study is examining a hypothetical scenario for VCPs, is the 60 elevation angle scenario practical for the listed update intervals of 2 and 5 minutes? This would require PPI scans every 2 or 5 seconds which is not possible with the XSAPR (but is with other X-band radar systems). Please elaborate on the technology limitation.

The referee is right. A volume scan with 60 elevations in less than 5 minutes is challenging for conventional scanning radars. The improvements required in the sampling strategy of the observing system (higher maximum elevation angle, higher density elevation angles and rapid VCP time period) can be accomplished using rapid scan radar systems such as the Doppler on Wheels mobile radars (DOWs, Wurman, 2001) or even phased array radar systems (e.g. Kollias et al, 2018). We added this description to the last paragraph in section 3.4 in the revised manuscript.

Figure 1: The Doppler velocity and spectrum with colors are saturated in a large portion of the figures. Suggest a wider colorbar range.

Done.

Technical Corrections: Line 280: Suggest “highly heterogeneous” instead of “high heterogenous”

Done.

Line 283: Suggest “between 10-minute intervals”

Done.

Line 302: Suggest “Each panel shows that CFPs at a single site”

Done.

Line 695: Extra comma in the data “May, 20, 2011”

Done. We removed a comma after “May.”

Figure 7 caption: units for cloud water mixing ratio should be g/kg

Done. Thank you for pointing the typo out.

Figure 9: Suggest “20-second output for 5 minutes” to be more clear in the Forward Model box

Done.

Anonymous Referee #2

The manuscript introduces a software (CR-SIM) for simulating ground-based radar and lidar observations, based on input from atmospheric models. The software itself is presented and several possible applications are demonstrated. Tools of this type are needed to e.g. plan measurement campaigns and evaluate models using real observations. Accordingly, there exist important objectives and the manuscript fits GMD well. As far as I can judge (with no direct experience of data of the type targeted by the software), the application examples are described sufficiently well. At least, the number of "use cases" is sufficiently high to convince a reader about the value of the software.

On the other hand, I find the description of the features and limitations of the software too short. I fully understand that not all details can be considered (but are hopefully covered by the user guide), but basic facts should be clarified in the manuscript, acting as the entrance points for potential users.

We thank the referee for their time and consideration reviewing the manuscript. We have revised the manuscript addressing all comments. Please see our point-by-point responses to the referee's comments.

1. First of all, it should more clearly be expressed how CR-SIM relates to similar software. Is there any other software that can do the same things as CR-SIM? Is CR-SIM unique in any way? Further, the use of "Finally" on line 84 gives the impression that the review of other software is complete, but I strongly doubt that is the case. For example, Matsui, T., Dolan, B., Rutledge, S. A., Tao, W.- K., Iguchi, T., Barnum, J., & Lang, S. E. (2019). POLARRIS: A POLARimetric Radar Retrieval and Instrument Simulator. *Journal of Geophysical Research: Atmospheres*, 124, 4634–4657. <https://doi.org/10.1029/2018JD028317> seems to have a similar scope as CR-SIM but is not mentioned.

Thank you for informing us about the paper to update the abstract citation originally used. In the revised manuscript, we refer to POLARRIS and this paper in Section 2 instead of Dolan et al. (2017) and added a sentence “Matsui et al. (2019) simulated polarimetric precipitation radar-based hydrometeor classification, vertical velocity, and rain rate from CRM output to examine uncertainties in the retrieval algorithms and model microphysical parameterizations using POLARRIS.”

We also compare CR-SIM with other simulators in section 4. Please see our response to referee #1's specific comment #1.

We agree with the referee that there are many other radar simulators and thus the list of existing software in this manuscript cannot be all-inclusive. We removed the word “Finally” and added “For example” to the beginning of the third sentence in Section 2.

2. The output variables should be better defined. For the radar ones (Table 2) not even the units are given. The dielectric factor used in the conversion to reflectivity can be defined in

different ways. Does CR-SIM allow different options, or what option is used? Equations or citations for the relationship between the scattering matrix elements and the output variables should be given (see e.g. Eqs. 1-16 in Matsui et al.). It is said that propagation effects are not treated. What is included in the term "propagation effects"?

The radar observables are computed by integrating scattering properties over the discrete PSD using a constant bin size for each hydrometeor. We followed the microphysical parameterization of the selected microphysics scheme to retrieve the PSD. The complex scattering amplitudes of the 2 x 2 scattering matrix are pre-computed for equally spaced particle sizes and stored in the look-up tables using the Mishchenko's T-matrix code for single non-spherical particles. Using the calculated scattering amplitudes stored in the LUTs, we computed radar observables following Ryzhkov et al. (2011), using for an assumption of the orientation distribution. CR-SIM incorporates three options of the orientation distribution model which can be selected by the user. The composition of particles is accounted for in the scattering computations by an appropriate selection of the dielectric constant for different hydrometeor types. The dielectric constant of liquid particles is frequency- and temperature-dependent (Ray, 1972). Ice phase hydrometeors are assumed to be made of ice inclusions in an ice matrix and their effective dielectric constant is computed using the Maxwell-Garnet mixing formula (1904). The output Z_{hh} is the equivalent radar reflectivity, in which computations, we adopt 0.92 as the value of dielectric factor for liquid water at centimeter wavelengths. This choice of the dielectric factor is dictated by convention to ensure that the definition of radar reflectivity reduces to form: $Z = \int N(D)D^6 dD$ for (spherical) liquid particles, where D is the droplet diameter and $N(D)$ is the droplet size distribution function.

The above information has been added to section 2 in the revised manuscript. Because the equations of radar observables have been well described in Ryzhkov et al. (2011), we decided to not add them in the manuscript. The method is fully described in the Section 4.4 and 4.5 in the CR-SIM User Guide (<ftp://ftp.radar.bnl.gov/outgoing/moue/crsim/docs/crsim-UserGuide-v3.3.0.pdf>).

We also added units for each output radar variable in Table 2 (now Table 3).

We meant “propagation effects” as the total attenuation along a radar beam path. We include specific attenuation from all simulated hydrometeors (i.e., cloud droplets, cloud ice, rain, snow, and graupel for the analysis in the manuscript), but gaseous attenuation was not included. We added the information in section 2.3.

3. Are there any other limitations that should be mentioned? As far as I understand, attenuation due to gases is not considered. That should be a significant effect at 94 GHz. Would be good to clarify if the attenuation due to liquid cloud droplets is included in the attenuation terms. Is the surface assumed to be flat or curved? Is refraction of importance? Ice particles seem to be treated as spheroids consisting of a mixture of ice and air. Just the choice of mixing rule (that is not specified) causes modelling uncertainties.

CR-SIM treats hydrometer categories for which mixing ratio (and/or number density) are provided by the input cloud model using the selected microphysics scheme. At this stage, all ice

hydrometeors (e.g., snow, ice, graupel, hail) are modeled as dielectrically dry spheroids i.e., assuming the dry growth of larger ice particles. Thus, the refractive index of ice-phase hydrometeors depends on relative mixture of air and solid ice and is computed using the Maxwell-Garnet mixing formula (1904). The LUTs of scattering properties incorporated in the current CR-SIM were created using the T-matrix method for selected assumptions regarding ice particle composition and shape. More complex electromagnetic scatters can be incorporated by adding LUTs of their scattering properties from different scattering calculation methods without any change to the code. We stated this in the revised manuscript in Section 2.1.

As in the response to the previous comment #2, we did not calculate gaseous attenuation in CR-SIM. We thank you for this suggestion. We will certainly add water vapor attenuation in a future version of CR-SIM.

In CR-SIM, the earth surface is assumed to be flat. This assumption is acceptable for shorter observation ranges. The description is added in section 2.3 in the revised manuscript. However, this could be a source of uncertainty for longer distances from the radar and/or for small model vertical grid spacings. We investigated the differences between the two assumptions (earth curvature + atmospheric refraction, and a flat surface). The figure below shows elevation angles at a height of 5.5 km AGL as a function of horizontal distance (right) and height at an elevation angle of 2° as a function of radar range (left). Here, the Earth's surface is represented using a sphere with a radius of 6370.0 km for red lines or flat for blue lines. The black lines represent the difference between the two assumptions. The difference in elevation angle is less than 1 degree for the horizontal distance less than 300 km at a fixed height. This is smaller than the elevation spacing of the scattering LUTs. At a fixed elevation angle, the difference in height is less than 1.4 km for the radar ranges < 150 km and is greater than 5 km at the radar range of 300 km. If the model vertical spacing is smaller than the difference, the error from the flat surface assumption could be significant. In the MCS simulation presented in the manuscript, the maximum radar range is 50 km for the X-band radars, and the model vertical resolution is approximately 250 m. For the shallow cumulus cases in the manuscript, the maximum radar range is 15 km and the model vertical resolution is 30 m. The differences at the maximum radar range for those cases are smaller enough than the model vertical spacings. However, we need to carefully configure the simulation settings considering the uncertainty. We thank the referee for their comment.

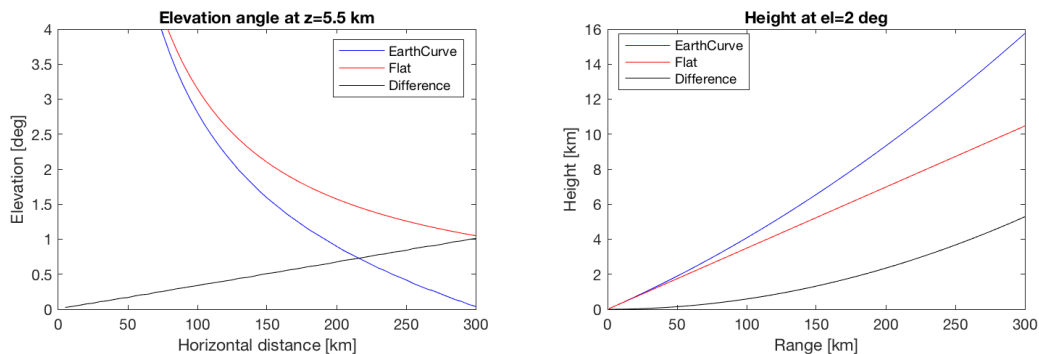


Figure 1: (Left) Elevation angle at a fixed height of 5.5 km AGL as a function of horizontal distance from the curved surface including the atmospheric refraction (blue) and flat surface (red) assumptions. (Right) Height at a fixed elevation angle of 2° as a function of radar range. Black

lines represent the difference between the two assumptions. The curved surface is assumed to be a sphere surface with a radius of 6370.0 km.

4. As a user, you need an estimate on the overall modelling uncertainty. For example, are differences between real observations and simulations of 3 dBZ significant or not?

There are several sources of uncertainty in CR-SIM including particle composition and shapes, particle size, and canting angles for the calculations of the single scattering properties. We have investigated the uncertainties in some of these assumptions. The figure below shows statistical differences of simulated radar observables between two particle shape assumptions: spheroidal ice (with an aspect ratio of 0.6) and spherical ice, using WRF+P3 model outputs. As expected, the aspect ratio assumption has the most influence on the polarimetric observables (i.e., Z_{DR} and K_{DP}). The influence is larger for the unrimed ice particles than for the partly-rimed ice particles.

As the referee pointed, the assumption of a flat Earth can also be an uncertainty source. Please see our response to the previous comment.

In addition, because CR-SIM ingests numerical model output, the assumptions in the microphysics schemes could also contribute to the uncertainty in CR-SIM. For example, the truncation of the edges of the PSDs (e.g., minimum and maximum sizes, size spacing) could affect CR-SIM results as pointed by referee#1. We added the settings of the PSD in Table 1 in the revised manuscript.

Since the input numerical model simulation itself can also include uncertainties, it is difficult to find an intrinsic uncertainty in CR-SIM by comparing the CR-SIM results with real observations. But comparisons with different radar simulator’s results can help to understand this uncertainty. One CR-SIM user compared the CR-SIM simulated reflectivity with reflectivity from another simulator (Passive and Active Microwave TRANSfer, PANTRA) for the same model input data. He reported differences in reflectivity ranging from 0.5 to 2 dB probably due to a difference of the diameter spacing implemented in the simulators.

We plan to summarize the uncertainty analyses in a follow-up paper.

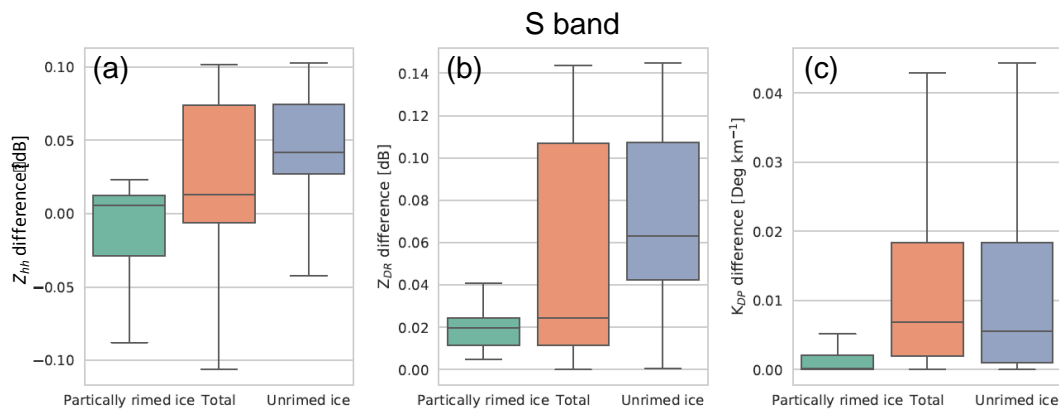


Figure 2. Box and whisker plots of the changes in (a) Z_{HH} , (b) Z_{DR} , and (c) K_{DP} by assuming spheroidal ice particles (aspect ratio = 0.6), compared to spherical particles (aspect ratio = 1.0)

with a fixed canting angle of 0 degree at a radar frequency of 3 GHz. The results are shown for ice categories (partly rimed ice, unrimed ice, and total ice) predicted by WRF P3 microphysics scheme for the mesoscale convective system simulation. Lower and upper box boundaries are 25th and 75th percentiles, respectively, the lines inside the box are medians, and the outermost lower and upper lines are 10th and 90th percentiles, respectively. The radar elevation angle is 20° for all simulations.

I found the manuscript hard to read due to the high usage of acronyms. Consider if some acronyms can be avoided, or adding a table of acronyms.

Thank you for this suggestion. We added a section with a list of acronyms.

Specific comments:

Line 88: What do you mean with "quality-controlled" and how do you ensure it?

Here, we mean ideal values of radar observables without observational limitations such as sensitivity, minimum detectable value, or hydrometeor attenuation. We realized that “quality-controlled” was a confusing word and used “ideal” instead in the revised sentence.

Line 94: T-matrix and DDA are general methods to calculate scattering properties, not scattering datasets. Is there any scattering dataset that could be coupled to your model?

We modified the phrase to read “scattering methods.” We added a description of the possibility to couple with different scattering calculation methods in section 2.1. Different scattering calculation datasets can be easily incorporated by adding LUTs of their calculated particle scattering properties (e.g., Kneifel et al., 2017; Leinonen and Moisseev, 2015; Leinonen and Szyrmer, 2015; Lu et al., 2016) without any change to the code. Please also see our response to the referee #1’s specific comment #1.

Line 108: How is bulk density defined?

The bulk density used is as parameterized in the selected microphysics scheme, assuming spheroidal particle shapes. Change made.

Line 138: Do you get the fall speed from the models, or by an external expression? If the later, add a reference.

We calculate the fall speed following the same manner as in the selected microphysics scheme in the models (given on L159). The parameterization depends on the microphysics schemes that are described in the references in (the now) Table 2 in the revised manuscript.

Lines 153-154: I don't get what you want to say what this sentence.

We revised the sentence to read "As expected, the lidar backscatter is significantly attenuated by cloud droplets, but the very high lidar backscatter at the interface between air a cloud can be used to detect cloud base height."

Line 196 and elsewhere: I don't think you can expect that all readers know the frequency of the radar bands (C, X, ...). At least define at the first usage of each band.

Thank you for the suggestion. We added the radar bands in text and figure captions.

Line 223: Start a new paragraph at "Figure 5 ..."

Done.

Line 238: "affects" -> "effects".

Done.

Lines 294-297: I could not understand this description.

We improved the paragraph. First, observation sites are randomly selected within the horizontal domain. Second, for each snapshot of the simulation, clouds over the observation sites are sampled as if the clouds are frozen in time and advected by the mean environmental wind. Thus, the columns are sampled along the direction of the horizontal wind over the advected distance (i.e. horizontal wind speed x 10 min), where the environmental horizontal wind at each snapshot is the mean horizontal wind across the simulation domain within the cumulus cloud layer (i.e., the layer between the mean cumulus cloud base and the maximum cumulus cloud top). Third and last, the CFP is estimated by varying both the number of observation sites and the integration period.

Line 331: Is CWRHI something built into CR-SIM, or done by external processing?

To simulate CWRHI accounting for radar beamwidth and range-gate spacing, a post-processing code is required. However, in the analysis by Oue et al. (2016), a CWRHI scan was referred to as a vertical cross section of CR-SIM simulated radar observables at the model grid. Figure 8 accounts for Z_{MIN} only. Details are described in Oue et al. (2016). To avoid the confusion, we revised the sentences in this paragraph.

Line 441: Is not the basic output from scanning radars in polar coordinates? If yes, is not this code essential to use CR-SIM and should then be fully integrated, as you claim that CR-SIM output "can be easily compared with real observations"?

The CR-SIM standard output is radar and lidar observables for all the cloud resolving model grid boxes accounting for elevation angles relative to a radar location, not polar coordinates that account for radar geometric characteristics such as beamwidth and radar range resolution to simulate scatters within the radar resolution volume. We describe this in Section 4 in the revised manuscript. The post-processing instrument model accounts for the radar sampling characteristics and outputs the observables in the polar coordinates. The post-processing code is now publicly available at the CR-SIM website (<https://you.stonybrook.edu/radar/research/radarsimulators/>) and also submitted to the Stony Brook University Academic Commons.

This feature facilitates the process of configuring any desirable observational setup with a varying number of profiling or scanning sensors and makes the gridbox-by-gridbox comparisons of the ideal radar variables easy.

Response to comments from Executive Editor

This is an executive editor comment highlighting the ways in which this manuscript is not currently compliant with GMD policy on code and data availability. In this case, there are a number of technical issues which needs to be remedied in the revised submission:

1. Model code on institutional websites. This is insufficiently persistent as institutional websites change. Please upload the exact version of the source code used to a persistent public archive such as Zenodo or the Stonybrook academic commons, and cite it appropriately. Since the code is GPL, there should be nothing preventing this from being done.

We have submitted the source code to the Stony Brook Academic Commons. The source code has been posted to the Stony Brook Academic Commons on December 9, 2019 at <https://commons.library.stonybrook.edu/somasdata/4>. We have updated the code availability in the revised manuscript. Because the source code is the latest version 3.3, we changed the title to “The Cloud Resolving Model Radar Simulator (CR-SIM) Version 3.3: Description and Applications of a Virtual Observatory.”

2. Code available on request. I recognise that this is quite a small piece of code, but it breaks the provenance chain for the paper. Please archive this code somewhere suitable (if it is really rather small then you might just include it in the supplementary material of the paper).

We posted the code that converts model grid coordinate to radar polar coordinate at the CR-SIM website on August 30, 2019. In addition, the code has been submitted to the Stony Brook Academic Commons together with the CR-SIM package (<https://commons.library.stonybrook.edu/somasdata/4>). We have updated the code availability.

3. The LASSO data used is not identified with sufficient precision that someone could reuse your work. The ARM archive provides a mechanism to generate a DOI for the exact data you want to cite. Please use this facility and cite the data following the instructions at <https://www.arm.gov/working-with-arm/acknowledging-arm/doi-guidance-for-datastreams>.

We have cited:

Atmospheric Radiation Measurement (ARM) Research Facility. September 2017. LASSO Data Bundles. , 36° 36' 18.0" N, 97° 29' 6.0" W: Southern Great Plains Central Facility (C1). Compiled by WI Gustafson, AM Vogelmann, X Cheng, S Endo, KL Johnson, B Krishna, Z Li, T Toto, and H Xiao. ARM Data Archive: Oak Ridge, Tennessee, USA. Data set accessed at <http://dx.doi.org/10.5439/1342961>.

4. The archive of configuration files is excellent, and the Stonybrook academic commons complies with GMD policy. However, citing this by URL is not good practice. If you look at the entry in the repository itself, it shows you how to cite it. Please do so: <https://commons.library.stonybrook.edu/somasdata/3/> Further details on code and data availability requirements are in the GMD model code and data policy:

https://www.geoscientific-model-development.net/about/code_and_data_policy.html. The reasons for the policy and more detail are provided in this editorial: <https://doi.org/10.5194/gmd-12-2215-2019>.

Thank you pointing this out. The data submission was posted on Oct. 4, 2019. We have included the right URL and citation in the revised manuscript.

List of author's changes in the manuscript taking account of referee's comments

1. Title

The current title: The Cloud Resolving Model Radar Simulator (CR-SIM) Version 3.3:

Description and Applications of a Virtual Observatory

2. Text

Major changes are:

- 1) Added a detailed description of scattering calculation (Section 2.1)
- 2) Added a description of computations of radar observables (Section 2.2)
- 3) Added a description of the instrument model (Section 2.3)
- 4) Revised sentences of simulation settings in Section 3.2, Section 3.4, and Section 4.
- 5) Added a list of acronyms after the summary section
- 6) Updated the code and data availability
- 7) Added proper references

3. Figures and Tables

- 1) Added Table 1. The minimum and maximum sizes and bin spacing of simulated particles for each hydrometeor category from the bulk microphysics schemes except the P3 scheme.
- 2) Added units to Table 3.
- 3) Revised Figure 1 and Figure 9.

The Cloud Resolving Model Radar Simulator (CR-SIM) Version 3.32: Description and Applications of a Virtual Observatory

Mariko Oue¹, Aleksandra Tatarevic², Pavlos Kollias^{1,3}, Dié Wang³, Kwangmin Yu⁴, Andrew M. Vogelmann³

- 5 1. School of Marine and Atmospheric Sciences, Stony Brook University, Stony Brook, 11794, USA
2. Department of Atmospheric and Oceanic Sciences, McGill University, Montreal, H3A 0G4, Canada
3. Environmental and Climate Sciences Department, Brookhaven National Laboratory, Upton, 11973, USA
4. Computational Science Initiative, Brookhaven National Laboratory, Upton, 11973, USA

Correspondence to: Mariko Oue (mariko.oue@stonybrook.edu)

10 **Abstract.** Ground-based observatories use multi-sensor observations to characterize cloud and precipitation properties. A challenge is how to design strategies to best use these observations to understand the atmosphere and evaluate atmospheric numerical prediction models. This paper introduces the Cloud resolving model Radar SIMulator (CR-SIM), which uses output from high-resolution atmospheric models to emulate multi-wavelength, zenith-pointing, and scanning radar observables and multi-sensor (multi-radar and radar-lidar) integrated products. CR-SIM allows comparisons of the same variables between an
15 atmospheric model simulation and remote sensing products using a forward modeling framework consistent with the microphysical assumptions used in the numerical model simulations. In this paper, we present several applications of CR-SIM for evaluation of a numerical model, quantification of retrieval uncertainty, and optimization of radar sampling strategy using observing system simulation experiments. These applications demonstrate that the application of CR-SIM as a virtual observatory operator on high-resolution model output helps interpret the differences between model results and observations
20 and also improve understanding of the representativeness errors due to the sampling limitations of the ground-based observatories. CR-SIM is licensed under the GNU GPL package and both the software and the user guide are freely available to scientific community.

1 Introduction

Ground-based observatories offer an integrated view of cloud and precipitation systems complementary to that available
25 from satellites with excellent vertical resolution, especially in the boundary layer, and an accompanying description of the large-scale forcing. Today, a number of observatories are continuously operated in different climate regimes (Illingworth et al., 2007; Löhnert et al., 2015; Stevens et al., 2016; Mather et al., 2016) with evolving measurement capabilities. In the beginning, zenith-pointing cloud radars, lidars, and radiometers provided the primary cloud and precipitation measurements. Recently, the need to characterize the mesoscale organization of clouds and precipitation over a larger domain has heightened
30 the sophistication and complexity of these observatories to go beyond single, one-dimensional profiling measurements. For

example, the U.S. Department of Energy (DOE) Atmospheric Radiation Measurement (ARM) observatories offer observations from distributed networks of profiling and scanning radars, lidars, and radiometers (Turner and Ellingson, 2016; North et al., 2017).

35 Multi-parametric information from profiling and scanning radars, lidars, and radiometers has been used to retrieve cloud
microphysical and kinematic properties, such as hydrometeor mixing ratio and number concentration (e.g., Zhang et al., 2014)
and ice particle properties (e.g., Kneifel et al. 2015; 2016; Matrosov et al. 2017; Von Lerber et al., 2017). However, the
comparison between the retrieved observables (e.g., ice water content (~~IWC~~) from radar reflectivity) and model-produced
parameters often involves large uncertainties. Several factors, not limited to the nature of ground-based observations, challenge
model evaluation using observations. In many cases, the retrieval algorithms are based on statistical estimation of ill-posed
40 inverse problems, and the results may not capture well the observed variability of natural data because of limitations from
assumptions embedded in the retrieval algorithms (e.g., Szyrmer et al., 2012; Szyrmer and Zawadzki, 2014). Furthermore,
determining critical parameters for model evaluation such as the cloud fraction profile requires complimentary, synergistic
observations from radar and lidar. One such example is the Active Remotely-Sensed Cloud Location (ARSCL, Clothiaux et
al., 2001) product that combines radar and lidar data to estimate hydrometeor location in the column. Other examples of critical
45 parameters that require a multi-sensor approach include cloud and precipitation classification schemes (Illingworth et al., 2007)
and hydrometeor phase classification (e.g., Shupe, 2007; Luke et al., 2010; Lamer et al., 2018). So, how do we best compare
such products developed using multiple sensors with different capabilities (i.e., sensitivity) with numerical model output?
Additionally, challenges may arise from the sampling strategy used to obtain the observations. For example, a recent study has
shown that profiling observations from one location are inadequate in representing statistically robust domain cloud properties
50 such as cloud fraction profile (Oue et al., 2016). A similar investigation on 3D wind retrievals in deep convection using multi-
Doppler radar techniques highlighted similar deficiencies of our current observing systems (Oue et al., 2019a). How do we
best quantify the measurement uncertainty introduced by the observational strategy?

In this paper, we introduce the Cloud Resolving Model (CRM) Radar Simulator (CR-SIM), which has been continuously
developed over the last five years to facilitate improvement of model-observation comparisons. CR-SIM applies forward
55 simulators to atmospheric model output to simulate sensor measurements. These sensor simulations may be used: (1) to
compare directly to the measurements, for an apples-to-apples comparison in sensor variables, or (2) as input to retrieval
algorithms to assess the retrieval methodology or sampling strategy using the original atmospheric model output as ‘truth.’
Here, the CR-SIM architecture and capabilities are presented along with a series of forward simulations that emphasize its
capabilities. In particular, we highlight the applications of CR-SIM in investigations of observational uncertainties (e.g., Potvin
60 et al., 2012). Although accurate estimation of uncertainties in the observation retrieval products (e.g., ~~IWC~~ice water content,
~~LWC~~liquid water content, vertical velocity) is challenging, forward simulators allow us to emulate the observational retrieval
products accounting for known error sources to understand the exact impacts of those error sources on the products by
comparisons with the ‘truth,’ which is usually the input model data. Observing system simulation experiments (OSSEs) take
advantage of forward modelling to produce simulated measurements. The understanding from OSSEs would help: i) evaluate

65 the model simulations using the observations accounting for the observation limitations, ii) estimate uncertainties in applied
retrieval techniques, iii) propose a new retrieval technique accounting for its uncertainty, and iv) optimize new observation
system strategy. This study demonstrates the application of the CR-SIM forward simulator in several OSSEs in which ARM
multi-sensor products, such as cloud locations and vertical velocity, are evaluated by considering limitations inherently
imposed by the nature of observations. [\(A list of acronyms is provided after the Summary for easy reference.\)](#)

70

2. Forward Simulators

Forward simulators have been widely used to design observing systems and to provide an alternative path to model-
observation comparisons by transforming the model geophysical quantities into remote sensing observables. There are several
sophisticated radar simulators, which have been developed for specialized applications of interest. [For example,](#) Snyder et al.
(2017a, 2017b) simulated polarimetric radar characteristics of a supercell using radar forward simulators to understand the
contribution of microphysical characteristics to the polarimetric characteristics and their wavelength dependency. They
accounted for the water fraction of solid ice particles to realistically simulate differential reflectivity (Z_{DR}) columns, specific
differential phase (K_{DP}) columns, and [co-polar correlation coefficient \(\$\rho_{hv}\$ \)](#) rings in supercells. A cloud radar simulator
developed by Zhang et al. (2018) is designed to simulate vertically pointing cloud radar reflectivity (e.g., Ka- and W-band
radars) from global climate model (GCM) data. This is beneficial for comparison of datasets of different scales (cloud-scale
observational data versus global-scale data). [Dolan-Matsui et al. \(20197\)](#) simulated ~~a~~-polarimetric precipitation radar-based
hydrometeor classification, [vertical velocity, and rain rate](#) from CRM outputs to examine uncertainties in the [retrieval](#)
[algorithms and model microphysical parameterizations using POLARRIS](#). The uncertainties are attributed to assumptions of
hydrometeor particle size distribution, density, axis ratio, and canting angle. ~~Finally,~~ Lamer et al. (2018) developed the GCM-
oriented ground-observation forward-simulator ((GO)²-SIM), a comprehensive radar-lidar simulator for GCMs, that emulates
radar Doppler spectra moments, lidar backscatter and depolarization, and provides synthetic estimates of mixed-phased cloud
occurrence in the GCM that are compared to those estimated from observations using the same methodology.

CR-SIM has the capability of simulating the [quality-controlled ideal](#) and propagation-corrected multi-wavelength radar
and lidar observables, and multi-sensor integrated products. The zenith-pointing and scanning radar observables include radar
reflectivity, Doppler velocity, [spectrum width,](#) and polarimetric fields. Zenith-pointing lidar observables include lidar
backscatter and extinction coefficient. The idea behind CR-SIM is to have a forward model operator that provides *idealized*
radar and lidar observables (i.e., actual observations after perfect quality control and correction ~~of for~~ the propagation effects)
on the same grid as in the CRMs or large-eddy simulations (LESs) to facilitate model-observation comparisons. Further, the
design is flexible enough to be coupled with different microphysical schemes and different scattering [datasets-methods](#) (e.g.,
T-matrix, Mishchenko, 2000; Discrete Dipole Approximation, Yurkin and Hoekstra, 2011).

The CR-SIM forward simulator is tailored to compute radar and lidar observables by integrating scattering properties over
the [discrete](#) particle size distributions (PSDs) [by a constant bin size](#) for each hydrometeor ([Table 1](#)), based on the microphysical

scheme ~~incorporated-used~~ in the CRM/LES. The environmental variables are obtained/calculated from a mandatory set of model output variables consisting of pressure, temperature, dry air density, and height above sea level. The single-scattering properties are calculated using the T-matrix method and packaged as look-up tables (LUTs) in CR-SIM. The simulated idealized radar and lidar variables are provided at each model grid box and can be easily compared with real observations.

2.1. Scattering Properties

The LUTs compile the complex scattering amplitudes of the 2 x 2 scattering matrix for single non-spherical particles with equally spaced particle sizes computed using the T-matrix code of Mishchenko and Travis (1998) and Mishchenko (2000). The LUTs for each hydrometeor class corresponding to the CRM/LES simulation data (e.g., rain drop, snowflakes, cloud droplet, ice crystal, graupel) are constructed as a function of particle phase, bulk density, and aspect ratio. The bulk density used is as parameterized in the selected microphysics scheme, assuming spheroid particle shapes. Hydrometeor particles considered in CR-SIM are liquid only or mixture of ice and air. For each hydrometeor class, the complex scattering amplitudes are calculated for the 91 elevation angles from 0° to 90° with a spacing of 1°, five radar frequencies at (3 GHz (S band), 5.5 GHz (C band), 9.5 GHz (X band), 35 GHz (Ka band), and 94 GHz (W band), different temperature ranges for the liquid hydrometeors, different particle densities for solid hydrometeors, and few different values of particle aspect ratio. For lidar scattering properties, the single particle extinction σ_{α} and backscattering cross section σ_{β} for spherical cloud droplets and cloud ice are calculated using the BHMIE Mie code (Bohren and Huffman, 1998). CR-SIM operates for observables from the ceilometer (wavelength of 905 nm) and micro pulse lidar (MPL, wavelengths of 353 and 532 nm).

Although most of the parameters related to hydrometeor particles (e.g., particle bulk density, size) required in the scattering calculations can be either computed or obtained from the prognostic and diagnostic variables from the CRMs or LESs, aspect ratios and canting angles must be assumed in the simulator and as such are prescribed by the users. All liquid and ice hydrometeors are modeled as oblate spheroids, except cloud droplets. Raindrops are represented as oblate spheroids with a size-dependent aspect ratio, following an empirical equation as a function of particle diameter based either on Brandes et al. (2002) or Andsager et al. (1999). A fixed aspect ratio is used for each solid hydrometeor category, but for graupel and hail the empirical expression proposed by Ryzhkov et al. (2011) is also available. Radar polarimetric variables depend on particle orientation, which is not information provided directly by the CRMs/LESs. For all model hydrometeors, the scattering amplitudes radar variables are calculated using complex scattering amplitudes from the pre-built LUTs, assuming a mean particle canting angle of 0° (Ryzhkov 2001) with a choice of the particle orientation distribution. The possible choices for the distribution of particle orientation model are fully (three-dimensional) random orientation, random orientation in the horizontal plane, and two-dimensional axisymmetric Gaussian distribution of orientations. In this paper, for all simulations, we used aspect ratios proposed by Brandes et al. (2002) for rain drops, 0.2 for cloud ice, 0.6 for snow, Ryzhkov et al. (2011) for graupel and hail, and the two-dimensional axisymmetric Gaussian distribution for all hydrometeor species.

135 A hydrometeor particle in CR-SIM is either pure liquid or a mixture of ice and air. The composition of particles within a volume is accounted for in the scattering computations by an appropriate selection of the dielectric constant for different hydrometeor types. The dielectric constant of liquid particles is frequency- and temperature-dependent (Ray, 1972). Ice phase hydrometeors are assumed to be composed of ice inclusions in an ice matrix and their effective dielectric constant is computed using the Maxwell-Garnet mixing formula (Maxwell Garnet, 1904). The output radar reflectivity (Z_{hh}) for all hydrometeor species is the equivalent radar reflectivity, in which computations, we adopt 0.92 as the value of dielectric factor for liquid water at centimeter wavelengths. This choice of the dielectric factor ensures a convention that the definition of radar reflectivity reduces to form: $Z = \int N(D)D^6 dD$ for (spherical) liquid particles, where D is the droplet diameter and $N(D)$ is the droplet size distribution function.

140 The LUTs of scattering properties incorporated in the current CR-SIM were created using the T-matrix method where solid phase hydrometeors are represented as dielectrically dry oblate spheroids. Although these assumptions are rather simple compared to some other radar simulators, which take into account complex electromagnetics scattering by mixed-phase hydrometeors or ice hydrometeors with possibly irregular shapes are taken into account (e.g., Snyder et al., 2017a,b; Jiang et al., 2019), such complex electromagnetic scatters can be easily incorporated by adding LUTs of their scattering properties from different scattering calculation methods (e.g., Kneifel et al., 2017; Leinonen and Moisseev, 2015; Leinonen and Szyrmer, 2015; Lu et al., 2016) without any change to the code.

150 2.2. Calculations of radar and lidar observables

155 The PSD for each hydrometeor species is reproduced on the basis of the model microphysics scheme. The incorporated microphysics schemes and corresponding CRMs currently available in CR-SIM are listed in Table 24. CRMs coupled with bulk moment microphysics (i.e., single and double moment) basically prognose mixing ratio and, for the double moment, the number concentration of each hydrometeor species. These parameters, in combination with assumptions used in the size distribution assumptions of the microphysics scheme, determine the PSD. Bin microphysics schemes explicitly calculate the evolution of the PSDs. Radar moment observables are computed by integrating scattering properties from the LUTs over the discrete PSD for each hydrometeor type following Ryzhkov et al. (2011) accounting for an orientation distribution as described in section 2.1, and then integrated over all simulated hydrometeor species to produce a unique value for each observable at each grid box. Particle fall velocity, which is used for Doppler velocity and spectrum width computations, is parameterized as a function of particle diameter in the same manner as in the selected microphysics scheme. Computed radar variables are listed in Table 32. Figure 1 shows an example of S-band (3 GHz) radar observables from CR-SIM for a mesoscale convective system (MCS) observed on May 20, 2011, during the Midlatitude Continental Convective Clouds Experiment (MC3E; Jensen et al., 2016). The convective system was simulated using the Weather Research Forecasting (WRF) model (Skamarock et al., 2008) with the Morrison 2-moment microphysics scheme, a horizontal resolution of 0.5 km, and the vertical resolution of approximately 0.25 km.

CR-SIM includes a computation of the Doppler power spectra by introducing the method used in Kollias et al. (2014). Figure 2 shows examples of the Doppler spectra and its moments for the S band. In the figure, a pulse repetition frequency (PRF) of 600 Hz is used, the noise power at 1 km is -40 dB, and the number of Doppler velocity bins is 256.

CR-SIM also includes forward simulators for the ceilometer (wavelength of 905 nm) and ground-based micro pulse lidar (wavelengths of 532 and 353 nm). The lidar observables are computed for cloud ice and cloud droplet species (see Table 43). Figure 3 shows an example of profiles calculated for lidar observables for a cumulus case from the LES ARM Symbiotic Simulation and Observation project (LASSO, Gustafson et al., 2017) using WRF coupled with the Morrison 2-moment microphysics scheme. In this simulation, typical profiles are presented for aerosol backscatter (β_{aero}) and extinction coefficient (α_{ext_aero}), and molecular backscatter (β_{mol}) based on Spinhirne (1993). As expected, the lidar backscatter the very high lidar backscatter near the cloud base height can help detect the cloud layer but is significantly attenuated by cloud droplets, but the very high lidar backscatter at the interface between air a cloud can be used to detect cloud base height.

2.3 Instrument model

The instrument model accounts for the effects of technological specifications on the observables, such as sampling volume and detector sensitivity. The standard output of CR-SIM consists of synthetic profiling radar and lidar observations at each grid box of the model scene, and synthetic scanning radar observations for a radar positioned at user's desired location inside the model domain. The output synthetic fields are artifact free, with no propagation or instrument sampling effects (~~assuming that the antenna and range weighting functions are delta functions at each grid box~~). This approach is based on the notion that the real observations used for comparison against the synthetic simulated observables will have undergone rigorous post-processing that mitigate to the extent possible propagation effects, velocity folding etc. However, the user can emulate the true behavior of a scanning radar and also select where to place the radar or a network of radars within the model domain and, thus, impose preferred volume coverage pattern (VCP) scan strategy. In this case, the idealized, standard CR-SIM output at the model grid resolution can be further used as input into a radar instrument model that is written specifically for the post-processing of the CR-SIM radar simulations. The radar instrument model accounts for radar distance to the target, elevation as provided by the VCP, pulse length, range resolution, antenna beamwidth, and receiver noise and output the radar observables in radar polar coordinates. For the calculation of elevation angles, the earth surface is assumed to be flat. This assumption is acceptable for general radar observation ranges (<~90 km for the vertical model grid spacing of >0.5 km). Gaussian functions ~~The antenna weighting and the range weighting function~~ are used as the antenna weighting and the range-weighting functions to estimate the contribution of the model grid observables to the radar polar coordinate system observables. Depending on the azimuthal resolution and the antenna beamwidth, this instrument model also accounts for the radar sampling resolution.

The radar instrument model in its current version does not treat propagation effects. Attenuated radar reflectivity can be computed using the integrated attenuation along a radar beam path. The total (two-way) hydrometeor attenuation (A_{tot}) at each

200 grid box is then equal to twice the sum of the specific attenuation for all simulated hydrometeors (A_h) along a radar beam path from the location of the radar to a distance of the target at r in km:

$$A_{tot}(r) = 2 \int_0^r A_h(r) dr \quad (1)$$

205 where A_{tot} is in dB and A_h in dB km⁻¹. Here gaseous attenuation was not included. The observed reflectivity Z_{hh}^{obs} (logarithmic scale) is computed by subtracting A_{tot} from Z_{hh} on a logarithmic scale:

$$Z_{hh}^{obs}(r) = Z_{hh}(r) - A_{tot}(r) \quad (2)$$

210 As well as Z_{hh} , the attenuated differential reflectivity Z_{DR}^{obs} on a logarithmic scale is calculated as:

$$Z_{DR}^{obs}(r) = Z_{DR}(r) - 2 \int_0^r A_{dp}(r) dr \quad (3)$$

215 where A_{dp} represents specific differential attenuation in dB km⁻¹. The minimum detectable reflectivity Z_{MIN} (logarithmic) is applied with a constant C :

$$Z_{MIN} = C + 20 \log_{10}(r) \quad (4)$$

where r is the radial distance in km, and the constant C represents the minimum detectable signal at $r = 1$ km for the pulse length selected by the user.

220 Figure 4 shows simulated range-height indicator (RHI) measurements at C and X bands (5.5 and 9 GHz, respectively) accounting for Z_{MIN} , hydrometeor attenuation, and the radar range-gate sampling volume for convective cells associated with an MCS observed on May 20, 2011 during MC3E. The input convective system simulation data are the same as Figure 1. The instrument specifications used for the RHI simulations are for the X-band radar, a beamwidth of 1°, range-gate spacing of 50 m, and a constant C of -50 dBZ for the Z_{MIN} calculation. The C-band radar specifications are a beamwidth of 1°, range-gate spacing of 120 m, and a constant C of -35 dBZ for the Z_{MIN} calculation. These specifications follow the X-band scanning ARM precipitation radar (X-SAPR) and C-band scanning ARM precipitation radar (C-SAPR) configurations at the ARM Southern Great Plains (SGP) site during MC3E. The results are reasonable, showing strong attenuation in Z_{hh} and Z_{DR} by rain at X band and relatively less at C band. The simulated K_{DP} at X band is approximately 1.6 times larger than that at C band because of the wavelength dependency.

230

2.4. Features of the Code

CR-SIM is written in Fortran 95 standard including all GNU extensions and parallelized with OpenMP. The input to CR-SIM is the output from the CRM/LES in NetCDF format. The output of CR-SIM is in NetCDF format and includes simulated observables for each hydrometeor specie, and one total for all the hydrometeors. These features allow users to understand contributions of each hydrometeor specie to the radar observables and a sophisticated evaluation of microphysics schemes. The code includes various microphysics schemes as shown in Table 34. The code structure supports different CRMs/LESSs, flexible microphysics package extensions, and diverse assumptions such as particle shape, density, and PSD for different hydrometeor categories in the models as well as different methods used for the computation of the scattering properties. The code has been released under GNU General Public License and both the software and a detailed user guide are publicly available online (Tatarevic et al., 2018).

3. Sample Applications of CR-SIM

In this section, several applications of CR-SIM are presented that highlight its capabilities. These applications are: i) a comparison of observed and modeled cloud fraction profiles (CFPs); ii) a quantification of uncertainty in the estimate of domain-averaged CFP; iii) an evaluation of a novel retrieval technique for the estimation of cloud fraction (CF); iv) an investigation of the impacts of limitations imposed by the nature of observations themselves on multi-Doppler wind retrieval techniques; and v) an optimization of a new radar observation strategy for multi-Doppler wind retrievals.

Figure 5 shows a flow diagram of our application processes. First, the forward simulator produces idealized observables at each model grid box (the ‘Output 1’ box in Figure 5). In the second step, an instrument model is used to account for the instrument characteristics (as described in section 2.3). Third, the output from the instrument model (‘Output 2’) is then used to retrieve the CFP (the retrieval model and ‘Output 3’) for a direct comparison and, most importantly, for a quantification of the uncertainties in the cloud fraction estimates, and as well for an evaluation of the new retrieval technique (applications i – iii). On another hand, the output from the instrument model is also used as an input for multi-Doppler wind retrieval model to investigate the uncertainty of the retrieval method itself and to optimize the new radar observation strategy (applications iv and v, with ‘Output 3’). The final step consists of a comparison of the retrieved quantities using a multi-Doppler wind retrieval against the input CRM/LES data, and a quantitative estimation of uncertainties attributed to the observation limitations and the retrieval algorithms. In the following subsections, we briefly describe and summarize the findings of the studies using CR-SIM.

3.1 Comparison of observed and modeled cloud fraction profiles

Measurements of the CFP are important to quantify the impact of shallow cumulus clouds on the grid-scale meteorological state because the fractional cloudiness of a grid box is related to effects in the radiative transfer (e.g., Albrecht 1981; Larson

265 et al., 2001) and the vertical cumulus mass flux (e.g., de Roode and Bretheton, 2003; van Stratum et al., 2014). Zenith-profiling
cloud radar and lidar measurements traditionally have been used to provide CFP estimates (e.g., Hogan et al., 2001; Kollias et
al., 2009; Remillard et al., 2013; Angevine et al., 2018). Typically, the profiling radar and lidar observations are combined
synergistically to provide a hydrometeor mask such as those described in ARSCL (Clothiaux et al., 2000) and the CloudNet
270 target classification (Illingworth et al., 2007). This approach takes advantage of the radar and lidar capabilities and maximizes
our ability to detect thin cloud layers. However, the performance of the combined radar/lidar algorithm degrades at heights
where the lidar observations are unavailable due to complete signal attenuation. These attenuation effects are naturally not
represented in model output and thus may lead to large disagreements between observations and models.

We focus here on using CR-SIM to generate a synthetic ARSCL product that is directly comparable to the ARSCL
generated using measurements from the Ka-band ARM Zenith-pointing Radar (KAZR), ceilometer, and MPL. This analysis
275 uses a shallow cumulus cloud field over SGP simulated by the ~~LES-ARM Symbiotic Simulation and Observations (LASSO;~~
~~Gustafson et al. 2019)~~ project. The simulation is for June 27, 2015 and uses WRF run as an LES coupled with the Morrison
double moment microphysics scheme (Morrison et al. 2005). The horizontal and vertical resolutions are 100 m and 20 m,
respectively, and the horizontal dimension of the simulation domain is 14.4 km.

First, the KAZR, ceilometer, and MPL measurements from the ARM SGP Central Facility are simulated using the CR-
280 SIM forward simulator. The simulation output corresponds to the box ‘Output 2’ in Figure 5. Simulated KAZR reflectivity
accounts for attenuation (Z_{hh}^{obs}) and radar sensitivity (Z_{MIN}) as described by Eqs. (1, 2, and 4). The attenuated MPL hydrometeor
backscatter (β_{hydro_atten}) is obtained by subtracting β_{aero_atten} and β_{mol_atten} from β_{total_atten} , since the MPL total backscatter includes
aerosol backscatter and molecular backscatter (see Table 43). The ~~value~~ obtained ~~for value~~ β_{hydro_atten} is considered to be below
noise level if less than the unattenuated background scatter ($\beta_{aero} + \beta_{mol}$), which is used in this simulation as the minimum
285 detectable MPL backscatter value. The ceilometer-detected first cloud base is estimated at each grid column following
O’Connor et al. (2004). Using the simulated observables, we estimate cloud locations as provided by ARSCL (‘Output 3’ in
Fig. 5). A grid box where either KAZR Z_{hh}^{obs} or MPL β_{hydro_atten} has a detectable value is indexed as a ‘cloudy’ grid box, and
grid boxes below the simulated ceilometer first-cloud base are indexed as ‘clear’.

An example of ARSCL simulation is shown in Fig. 6 that uses the LASSO LES data as an input. The WRF simulation
290 shows cumulus clouds below 5 km and cirrus clouds covering the entire domain at 12-14 km. In Figs. 6b-d, the limitation of
each instrument is represented in the forward simulations. The simulated KAZR measurements can detect cumulus cloud layers
but cannot detect cirrus clouds, due to their low reflectivity (lower than Z_{MIN}). Instead, the cirrus clouds can be detected by the
simulated MPL measurements. However, the cirrus clouds can be missed by both radar and lidar measurements when cumulus
clouds are present, because the MPL signal becomes fully attenuated by the low-level clouds. Figures 6f and 6g show the
295 domain-averaged CFPs from the LES hydrometeor mixing ratio and from the simulated ARSCL which assumes the ARM
instruments are located at every grid column (as shown in Fig. 6e). Comparison between the two CFP plots suggests that the
ARSCL for this LASSO case underestimates cirrus CFPs by 20%, likely due to lidar beam attenuation by lower-level cumulus
clouds that have a horizontal fraction of 20%.

300 3.2 Uncertainty quantification of domain-averaged cloud fraction profile estimates

The ARSCL product is usually integrated for 1-3 hours to provide an average CFP estimate for that time period. These CFP estimates are often compared with the model domain-averaged CFPs. However, the spatially heterogeneous distribution of the shallow cumulus clouds (Wood and Field, 2011) raises questions regarding the ability of short-term (1–3 hours) zenith-
305 profiling observations to provide adequate sampling of the cloud field. Uncertainties in the profiling measurement of cloud fractions are introduced by the limited sampling of a highly heterogeneous cloud field. We investigate these uncertainties as a function of the number of profiling sites and integration time using the CR-SIM virtual observations, using the WRF LES simulation presented in the previous application. The ~~WRF simulation-LES~~ output is saved every 10 minutes, ~~and CR-SIM is run for each output file~~. In this analysis, we assume that no cloud evolution occurs ~~within a 10-10-minute interval~~.

310 Figures 7a and 7b show the domain-averaged CFP from the simulated ARSCL and directly from the WRF using a cloud water content threshold of 0.01 g kg^{-1} . The color ~~shades~~ indicate different integration time periods. Note that the WRF dataset in this analysis is for a SGP shallow convective cloud case on June 11, 2016, different from the one used in Fig. 6, which results in higher cumulus cloud top. The simulated ARSCL CFP is in good agreement with the WRF CFP for each integrated period (compare Figs. 7a and b), indicating that uncertainties attributed to observation limitations (e.g., sensitivity and
315 attenuation) are small. Thus, the limited spatial and/or temporal sampling is the major error source ~~we should to~~ consider when comparing the profiling measurement derived CFP with the domain-averaged WRF CFP.

To emulate vertical profiling measurements, we sampled data as follows. First, observation sites are randomly selected within the horizontal domain. Second, ~~for each snapshot of the simulation, simulated~~ clouds ~~over the observation sites are sampled as if the clouds are frozen in time and advected by the mean environmental wind. Thus, the columns are sampled~~
320 ~~along the direction of the horizontal wind over the advected distance (i.e. horizontal wind speed \times 10 min), where in each column are sampled according to the distance that clouds are advected in the direction of the environmental horizontal wind during 10 minutes (i.e. horizontal wind speed \times 10 min).~~ The environmental horizontal wind at each snapshot is the mean horizontal wind across the simulation domain within the cumulus cloud layer (i.e., the layer between the mean cumulus cloud base and the maximum cumulus cloud top). Third and last, ~~the sampled data are integrated over time and~~ the CFP is estimated
325 by varying both the number of observation sites and the integration period.

Figures 7c-h show the comparisons of the WRF CFPs and the simulated ARSCL CFPs for different number of observation sites (top row, c-e) and integration periods (bottom row, f-h). The center of integration period is 21:00 UTC. Blue lines in each panel represent the simulated ARSCL CFPs integrated over time from each selected observation site for the period indicated, the red line represents the mean ARSCL CFP averaged over the sites, and the black line represents the domain-averaged WRF
330 CFP integrated over the indicated period. Each panel shows that CFPs at a single site (blue lines) have large uncertainties even though they are integrated over long periods, ranging from 30 to 180 min. Those uncertainties are reduced when averaging the CFP profiles across the different sites; consequently, the mean CFP (red line) becomes closer to the domain-averaged WRF

CFP (black lines). However, it also becomes evident that a small number of observation sites (Fig. 7c) may not be adequate to estimate the true CFP.

335 Figures 7i and 7j show the root mean square error (RMSE) and mean absolute percentage error (MAPE) of the simulated ARSCL CFPs as a function of the number of observation sites and the integration time. Both plots show that the uncertainty can be reduced by increasing the number of observation sites and the integration period. The RMSE dramatically decreases to 0.005-0.01 (30-50 % in MAPE) when we use four observation sites and 120 min integration. The rate of improvement of CFP by further increasing the number of sites and integration period is smaller; the error values slowly decrease until the RMSE and MAPE plateau at 0.002 and 15%, respectively. However, establishing more than ten observational sites in such small domain is probably impractical. At the SGP site, five Doppler Lidar profiling measurements have already been operating over a 90 km x 90 km domain. These measurements can be effectively used to estimate cloud fraction without much uncertainty when clouds are homogeneously distributed over the domain.

345 3.3 Evaluation of a new CFP estimation technique using scanning cloud radar

Forward radar simulators can be used to evaluate a retrieval technique. We introduce an application to estimating CFP using scanning cloud radar (SCR) measurements based on Oue et al. (2016). As analyzed in the previous section, profiling radar measurements may include large uncertainties in CFP estimates. On the other hand, SCRs conduct observations over a domain that is much larger than can be sampled by zenith-profiling cloud radars such as ~~KAZR the Ka-band ARM Zenith Radar (KAZR, e.g., Lamer et al., 2013; Ewald et al., 2015)~~. Although the SCRs are widely and routinely used to observe 3D cloud fields, the application of SCRs to study shallow cumuli is not straightforward. One of the most significant limitations of the SCR observations is related to the radar sensitivity. Since shallow cumuli over land typically have low reflectivities, the strong drop in SCR sensitivity with range creates the illusion of the atmosphere being cloudier closer to the radar location (e.g., Lamer and Kollias, 2015). This limitation can introduce uncertainties in the cloud fraction estimates. Oue et al. (2016) addressed uncertainties of radar-estimated CFPs due to the nature of the profiling and scanning radar techniques using CR-SIM-generated observations.

Figure 8a shows horizontal cross sections of WRF-simulated water content for a shallow convection case (June 9, 2015; Oue et al., 2016) from LASSO. Figure 8b shows the CR-SIM simulation of the Ka-band (35 GHz) Z_{hh} ~~from a cross-wind RHI scan (CWRHI, Kollias et al., 2014) which~~ accountings for the minimum detectable reflectivity Z_{MIN} ~~of the cross-wind RHI (CWRHI, Kollias et al., 2014) scans from Eq. (4) using $C=-50$ dBZ~~. In the CR-SIM analysis, the radar was located along the vertical line in Figure 8b, and CWRHI scans were performed along the east-west direction while the clouds were assumed to move along the north-south direction. ~~These figures The simulated CWRHI observations show~~suggest that the Z_{hh} from the CWRHI scans cannot capture the clouds with lower water contents that are located far from the radar. This can affect cloud fraction estimates. Since the “true” cloud fraction is estimated from the original model cloud field and thus is known, the CR-SIM runs in different configurations can be used to establish the best method to estimate cloud fraction while accounting for

370 limitations inherent to the nature of radar measurements. Oue et al. (2016) used the cumulative distribution function (CDF) of the observed Z_{hh} to define the size of the horizontal domain at each height needed to obtain the best estimate of the domain-averaged CFP. The horizontal domain size as a function of height corresponded to a distance from the radar where Z_{MIN} was equal to a CDF value of 10%. Figure 8c shows CFPs using a CDF of 10% when changing the integration time of the CWRHI, and Figure 8d shows the RMSE of the estimated CFPs as a function of integration time, adapted from Oue et al. (2016). The figure suggests that the 35 min or longer of CWRHI measurements provide the realistic domain-averaged CFP.

3.4 Investigation of impacts of observation limitations on multi-Doppler radar wind retrievals

375

Estimation of vertical air motion is essential to understand the dynamics and microphysics of deep convective clouds (e.g., Jorgensen and LeMone, 1989), evaluate CRM and LES results (e.g., Varble et al., 2014; Fan et al., 2017), and to improve convective parameterization in global climate models (e.g., Donner et al., 2001). Multi-Doppler radar techniques have been applied to understand the dynamics and microphysics of the deep convective clouds in different climate regimes (e.g., Friedrich and Hagen, 2004; Collis et al., 2013; Oue et al., 2014). However, the multi-Doppler radar retrievals are not straightforward with potential uncertainties from multiple aspects (e.g., Clark et al., 1980; Bousquet et al., 2008; Potvin et al., 2012). CR-SIM can be used to investigate the impacts of different error sources on the retrieved wind fields.

380

385

Oue et al. (2019a) investigated the impacts of the radar ~~volume coverage pattern~~ (VCP) for plan position indicator (PPI) and the observation period on uncertainties in multi-Doppler radar wind retrievals using CR-SIM. They also investigated how the uncertainties attributed to the VCP period can be reduced using ~~the an~~ advection-correction technique proposed by Shapiro et al. (2010). The advection correction scheme allows for trajectories of multiple individual clouds, performs smooth gridbox-by-gridbox corrections of cloud locations, and takes into account changes in cloud shape with time by using PPI scans at two times. We summarize their findings, particularly regarding the impacts of radar VCP and period on multi-Doppler radar retrievals.

390

395

Figure 9 shows a diagram of the analysis process. The input model data is a WRF simulation using the Morrison double-moment microphysics scheme for a mesoscale convective system observed on May 20, 2011, during the MC3E field campaign at the ARM SGP site. The horizontal resolution is 500 m, the vertical resolution varies from approximately 30 m near the surface to 260 m at 2 km—above which the resolution remains approximately constant, and the simulation output is saved every 20 seconds. Measurements from the three X-band scanning ARM precipitation radars (X-SAPR) at the SGP site are simulated using CR-SIM. The CR-SIM-simulated radar reflectivity and Doppler velocity at the model grid are converted into the radar polar coordinates with two different VCPs for each radar: 1) 21 elevation angles ranging from 0.5° to 45° (VCP1, same as the X-SAPR scan strategy during MC3E), and 2) 60 elevation angles ranging from 0.5° to 59.5° with a 1° increment (VCP2). For the both VCPs, the beamwidth is 1°, the range-gate spacing is 50 m, and the maximum range is 40 km. The simulated radar reflectivity and Doppler velocity in polar coordinates were used as an input to the 3DVAR multi-Doppler radar

400 wind retrieval algorithm developed by North et al. (2017) to estimate the 3D wind field for a domain of 50 km × 50 km × 10 km with horizontal and vertical grid spacings of 0.25 km.

The convective mass flux (MF) is estimated at each height as:

$$MF = UF \bar{w} \overline{\rho_d} \quad [kg \ s^{-1} \ m^{-2}] \quad (5)$$

405

where UF is updraft fraction over the horizontal slice of the domain, \bar{w} is mean vertical velocity over the updraft area, and $\overline{\rho_d}$ is dry air density averaged over the domain. Figure 10 shows comparisons of convective mass flux profiles between simulated multi-Doppler radar retrievals and WRF output for two minimum updraft thresholds of 5 (MF_5) and 10 (MF_{10}) $m \ s^{-1}$. First, we applied the wind retrieval technique to a snapshot of the forward model output to bypass the instrument model and examine the uncertainty in the retrieval model (3FullGrid). Figure 10a shows MF profiles from the 3FullGrid simulation (red line) and from WRF the snapshot (black line), 2-min average (dark gray line), and 5-min average (light gray line). The 3FullGrid MF profile is in good agreement with the WRF output which indicates that the uncertainty in the retrieval model is small; although it does underestimate the maximum MF for the updraft threshold of 5 $m \ s^{-1}$ by 0.05 $kg \ m^{-2} \ s^{-1}$ (10% of the true MF) at 5.3 km.

410

Figures 10b and 10c show MF profiles (MF_5 and MF_{10}) obtained from simulated retrievals while considering the effects of VCP (VCP1 and VCP2) and averaging period (snap [instantaneous], 2-min and 5-min averages). For both VCP1 (Fig. 10b) and VCP2 (Fig. 10c), the snapshot and 2-min VCP simulations have similar MF estimates for both sets of MF_5 and MF_{10} curves, indicating that a 2-min average is sufficient to capture features available from an instantaneous scan. However, the accuracy of these estimates varies with MF profile and VCP. The MF_{10} estimates for both VCPs systematically underestimate the maximum values occurring between 4.5-6.5 km by about 0.5 $kg \ m^{-2} \ s^{-1}$ (20%). The performance of the MF_5 estimates for VCP snap and 2-min have strong variations with height. For VCP1 (the less dense scan pattern), MF_5 follows the WRF snapshot below 4.5 km with close agreement between 3-4.5 km; however, MF is underestimated around its maximum MF by about 0.075 $kg \ m^{-2} \ s^{-1}$ (15%) and is overestimated below 3 km and above 7 km. The denser scan pattern for VCP2 provides a dramatic improvement around the maximum and above 6 km but still shows overestimations below 3 km and above 7 km. Uncertainties are often increased for the VCP simulations when the averaging period is extended to 5-min. For the 5-min VCPs, MF_{10} estimates for both VCP1 and VCP2 around the maximum are further underestimated while the MF_5 estimate for VCP2 is further overestimated above 6 km. Other estimates below this height for VCP2 and for all heights for VCP1 are mostly unchanged. These results suggest that the VCP elevation strategy and sampling time extended to 5 min have a significant impact on the updraft properties retrieved at higher altitudes. This is due to density of data sampled by the VCPs, where greater density particularly improves MF_5 around its maximum, and the deformation of cloud structures within longer sampling periods (exceeding 2 min) that causes uncertainties in the mass continuity assumption.

420

425

430

The rapid volume scan of less than 5 minutes required in the retrieval of the high-quality vertical velocities is challenging for conventional scanning radars. Most of the improvements required in the sampling strategy of the observing system (higher

maximum elevation angle, higher density elevation angles, and rapid VCP time period) can be accomplished using rapid scan radar systems such as the Doppler on Wheels mobile radars (DOWs, Wurman, 2001) or even phased array radar systems (e.g. Kollias et al, 2018).

3.5 Evaluation of new radar observation strategies

CR-SIM can also be used to examine performances of new remote sensing sensors and thus help to choose the most appropriate observation strategy for a new field campaign. Figures 4c and 4d show the performance of C-band (5.5 GHz) RHI measurements when the radar is located at 24 and 59 km away from the target convective clouds. As expected, the RHI from the greater distance provides the radar observables at lower resolution and includes more attenuation when precipitation clouds are located between the target and the radar. Oue et al. (2019a) investigated the impact of radar data sampling on the multi-Doppler radar wind retrievals for the MCS by an OSSE using CR-SIM. The addition of data from a Doppler radar to the triple-Doppler radar retrievals, shown in section 3.4, cannot significantly improve the updraft retrievals if the added radar VCP has inferior spatial resolution. Oue et al. (2019a) also showed that the updraft retrievals in a limited area around the center of the domain, where data density from the three radars are higher than other areas, produced better results than those in the entire domain. The insights obtained from these OSSEs are beneficial for decision-making regarding radar observation strategies for a field campaign, such as the number of radars required and their locations. For example, Kollias et al. (2018) used CR-SIM to examine how phased array radars improve multi-Doppler radar wind retrievals compared to scanning radars for mesoscale convective cases.

4. Summary

We presented a recently developed comprehensive forward radar and lidar simulator, CR-SIM, which is suitable for simulating complex, ground-based observational configurations and their synthetic products. CR-SIM can simulate multi-wavelength, zenith-pointing and scanning radar observables—including radar reflectivity, Doppler velocity, polarimetric fields, radar Doppler spectrum—lidar observables, and multi-sensor integrated products. The primary idea behind this simulator was to directly compare CRM/LES output with remote sensing observations such that simulated measurements are consistent with the microphysics scheme used in the model. CR-SIM incorporates microphysics and scattering properties independently so that uncertainties related to microphysical assumptions are separated from uncertainties related to scattering model. This configuration allows CR-SIM to be easily expanded, either by adding additional microphysical schemes or by adding new scattering classes.

One of the features of using CR-SIM is it produces both radar and lidar observables for all the cloud resolving model grid boxes accounting for elevation angles relative to a radar location, similar to Snyder et al. (2017a,b), rather than other radar simulators that account for radar geometry characteristics such as beamwidth and radar range resolution to simulate scatters

within the radar resolution volume (e.g., Capsoni et al, 2001; Caumont et al., 2006; Cheong et al., 2008). The radar sampling characteristics are accounted for in the post-processing instrument model. This feature facilitates the process of configuring any desirable observational setup with a varying number of profiling or scanning sensors. Another feature of CR-SIM is that it can be coupled to sophisticated virtual products such as ARSCL and 3DVAR multi-Doppler based wind retrievals. The CR-SIM applications shown in this paper emphasize the value of applying it to high resolution model output to emulate the sampling of ground-based observatories. CR-SIM's coupling of CRM microphysical parameterizations with scattering models facilitates improved evaluations of model performance by enabling robust comparisons between model-simulated clouds and observables from radar and lidar while accounting for instrument characteristics and observation limitations. The analyses presented here serve as a reference to the CR-SIM package and illustrate numerous applications related to sampling uncertainty, sampling optimization, retrieval uncertainty, and comparison between models and observations.

List of acronyms

ARM	<u>Atmospheric Radiation Measurement Facility</u>
ARSCL	<u>Active Remotely-Sensed Cloud Location</u>
480 CDF	<u>Cumulative distribution function</u>
CFP	<u>Cloud fraction profile</u>
CRM	<u>Cloud resolving model</u>
CR-SIM	<u>Cloud resolving model Radar SIMulator</u>
C-SAPR	<u>C-band scanning ARM precipitation radar</u>
485 CWRHI	<u>Cross-wind range-height indicator</u>
GCM	<u>Global climate model</u>
GNU GPL	<u>GNU General Public License</u>
KAZR	<u>Ka-band ARM Zenith-pointing Radar</u>
LASSO	<u>LES ARM Symbiotic Simulation and Observation</u>
490 LES	<u>Large eddy simulation</u>
LUT	<u>Look-up table</u>
MAPE	<u>Mean absolute percentage error</u>
MC3E	<u>Midlatitude Continental Convective Clouds Experiment</u>
MCS	<u>Mesoscale convective system</u>
495 MF	<u>Mass flux</u>
MPL	<u>Micro pulse lidar</u>
OSSE	<u>Observing system simulation experiment</u>
PPI	<u>Plan position indicator</u>
PSD	<u>Particle size distribution</u>

500	<u>RHI</u>	<u>Range-height indicator</u>
	<u>RMSE</u>	<u>Root mean square error</u>
	<u>SCR</u>	<u>Scanning cloud radar</u>
	<u>SGP</u>	<u>Southern Great Plains</u>
	<u>UF</u>	<u>Updraft fraction</u>
505	<u>VCP</u>	<u>Volume coverage pattern</u>
	<u>WRF</u>	<u>Weather Research Forecasting model</u>
	C-SAPR	C-band scanning ARM precipitation radar
	<u>X-SAPR</u>	<u>X-band scanning ARM precipitation radar</u>

510 **Code and data availability.**

The source code for CR-SIM, along with downloading, installation instructions, and user guide is available at [the Stony Brook University Academic Commons \(https://commons.library.stonybrook.edu/somasdata/4\)](https://commons.library.stonybrook.edu/somasdata/4), <https://www.bnl.gov/CMAS/cr-sim.php> (last access: ~~June 18~~[September 6, 2019](#)), and <https://you.stonybrook.edu/radar/research/radar-simulators/> (last access: ~~April~~[September 5, 2019](#)~~40~~). The software is licensed under GNU General Public License. A code that converts model grid coordinates to radar polar coordinates is [also available at the Stony Brook University Academic Commons](#) <https://commons.library.stonybrook.edu/somasdata/4> and <https://you.stonybrook.edu/radar/research/radar-simulators/> (last access: [August 30, 2019](#))~~upon request~~. There is ongoing work to integrate this module into the CR-SIM package. The CR-SIM package available online includes a configuration file and a script to run the code. The LASSO data used in the manuscript are available at the ARM archive: <https://adc.arm.gov/lassobrowser> (ARM, 2017). All configuration files used in the simulations and other input data available online <https://commons.library.stonybrook.edu/somasdata/3> (Oue et al. 2019b).

Author contributions.

M. Oue and P. Kollias designed the OSSE experiments, and M. Oue carried them out. A. Tatarevic developed the radar simulator code, and with M. Oue, D. Wang, and K. Yu contributed to evolve, improve, and optimize the code. M. Oue prepared the manuscript with contributions from all co-authors.

Competing interests.

The authors declare that they have no conflict of interest.

530

Acknowledgements.

We would like to thank H. Morrison, Z. Feng, J. Fan, T. Matsui, and S. Endo for providing the WRF output data and for their valuable suggestions. We extend our gratitude to M. Mech and A. Hansen, P. Marinescu, and T. Yamaguchi for providing the

ICON, RAMS, and SAM output data, respectively, and for their helpful comments. We would also like to thank ~~J. Vivekanandan for his Mueller matrix based code and~~ M. I. Mishchenko for making his T-matrix codes public and freely available for research purposes and J. Vivekanandan for his Mueller-matrix-based code, which was used to validate the computation of radar variables in CR-SIM. This research was supported by the Climate Model Development and Validation activity funded by the Office of Biological and Environmental Research in the US Department of Energy Office of Science through award KP170304 (P. Kollias and A. M. Vogelmann).

540 References

- Albrecht, B. A.: Parameterization of trade-cumulus cloud amounts. *J. Atmos. Sci.*, 38, 97-105, doi: 10.1175/1520-0469(1981)038<0097:POTCCA>2.0.CO;2, 1981.
- Angevine, W, Olson, J., Kenyon, J., Gustafson, W., Endo, S., Suselj, K., and Turner, D.: Shallow cumulus in WRF parameterizations evaluated against LASSO large-eddy simulations, *Mon. Wea. Rev.*, doi:10.1175/MWR-D-18-0115.1, 2018.
- Andsager, K., Beard, K. V., and Laird N. F.: Laboratory measurements of axis ratios for large drops, *J. Atmos. Sci.*, 56, 2673–2683, doi: 10.1175/1520-0469(1999)056<2673:LMOARF>2.0.CO;2, 1999.
- Atmospheric Radiation Measurement (ARM) Research Facility. September 2017. LASSO Data Bundles., 36° 36' 18.0" N, 97° 29' 6.0" W: Southern Great Plains Central Facility (C1). Compiled by WI Gustafson, AM Vogelmann, X Cheng, S Endo, KL Johnson, B Krishna, Z Li, T Toto, and H Xiao. ARM Data Archive: Oak Ridge, Tennessee, USA. Data set accessed at <http://dx.doi.org/10.5439/1342961>.
- Bohren, C. F. and Huffman, D. R.: Absorption and scattering of light by small particles, New York : Wiley, 1998, 530 p., ISBN 0-471-29340-7, ISBN 978-0-471-29340-8 (second edition).
- Bousquet, O., Tabary, P., and Parent du Châtelet, J.: Operational multiple-Doppler wind retrieval inferred from long-range radial velocity measurements, *J. Appl. Meteor. Climatol.*, 47, 2929-2945, doi: 10.1175/2008JAMC1878.1, 2008.
- Brandes, E. A., Zhang, G., and Vivekanandan, J.: Experiments in rainfall estimation with a polarimetric radar in a subtropical environment, *J. Appl. Meteor.*, 41, 674–685, doi: 10.1175/1520-0450(2002)041<0674:EIREWA>2.0.CO;2 2002.
- Capsoni, C., D'Amico, M., and Nebuloni, R.: A Multiparameter Polarimetric Radar Simulator. *J. Atmos. Oceanic Technol.*, 18, 1799–1809, [https://doi.org/10.1175/1520-0426\(2001\)018<1799:AMPRS>2.0.CO;2](https://doi.org/10.1175/1520-0426(2001)018<1799:AMPRS>2.0.CO;2), 2001.
- Caumont, O., Ducrocq, V., Delrieu, G., Gosset, M., Pinty, J., Parent du Châtelet, J., Andrieu, H., Lemaître, Y., and Scialom, G.: A Radar Simulator for High-Resolution Nonhydrostatic Models. *J. Atmos. Oceanic Technol.*, 23, 1049–1067, <https://doi.org/10.1175/JTECH1905.1>, 2006.
- Cheong, B.L., Palmer, R.D., and Xue, M.: A Time Series Weather Radar Simulator Based on High-Resolution Atmospheric Models. *J. Atmos. Oceanic Technol.*, 25, 230–243, <https://doi.org/10.1175/2007JTECHA923.1>, 2008.
- Clark, T. L., Harris, F. I., and Mohr, C. G.: Errors in wind fields derived from multiple-Doppler radars: Random errors and temporal errors associated with advection and evolution, *J. Appl. Meteor.*, 19, 1273–1284, 1980.
- Clothiaux, E. E., Ackerman, T. P., Mace, G. G., Moran, K. P., Marchand, R. T., Miller, M. A., and Martner, B. E.: Objective determination of cloud heights and radar reflectivities using a combination of active remote sensors at the ARM CART sites, *J. Appl. Meteor.*, 39(5), 645-665, doi: 10.1175/1520-0450(2000)039<0645:ODOCHA>2.0.CO;2, 2000.
- 570 Clothiaux, E. E., Miller, M. A., Perez, R. C., Turner, D. D., Moran, K. P., Martner, B. E., Ackerman, T. P., Mace, G. G., Marchand, R. T., Widener, K. B., Rodriguez, D. J., Uttal, T., Mather, J. H., Flynn, C. J., Gaustad, K. L., and Ermold, B.:

- The ARM Millimeter Wave Cloud Radars (MMCRs) and the Active Remote Sensing of Clouds (ARSCL) Value Added Product (VAP), DOE Tech. Memo. ARM VAP-002.1, 2001.
- 575 Collis, C., Protat, A., May, P. T., and Williams, C.: Statistics of storm updraft velocities from TWP-ICE including verification with profiling measurements, *J. Appl. Meteor. Climatol.*, 52, 1909-1922, doi: 10.1175/JAMC-D-12-0230.1, 2013.
- Cotton, W. R. et al.: RAMS 2001: Current status and future directions, *Meteorol. Atmos. Phys.*, 82(1), 5–29, doi:10.1007/s00703-001-0584-9, 2003.
- de Roode, S. R., and Bretherton C. S.: Mass-flux budgets of shallow cumulus clouds. *J. Atmos. Sci.*, **60**, 137–151, doi: 10.1175/1520-0469(2003)060<0137:MFBOSC>2.0.CO;2, 2003.
- 580 ~~Dolan, B., Rutledge, S. A., Barnum, J. I., Matsui, T., Tao, W. K., Iguchi, T.: Investigation of hydrometeor classification uncertainties through the POLARRIS polarimetric radar simulator, Abstract A34A-05 presented at 2017 Fall Meeting, AGU, New Orleans, LA, 11-15 Dec., 2017.~~
- Donner, L. J., Seman, C. J., Hemler, R. S., and Fan, S.: A cumulus parameterization including mass fluxes, convective vertical velocities, and mesoscale effects: Thermodynamic and hydrological aspects in a general circulation model, *J. Climate*, 14, 3444–3463, doi: 10.1175/1520-0442(2001)014<3444:ACPIMF>2.0.CO;2, 2001.
- 585 Doviak, R. J., and Zrníc, D. S.: Doppler radar and weather observations, 2nd ed., San Diego, Academic Press, Second Addition, 2006.
- Ewald, F., Winkler, C., and Zinner, T.: Reconstruction of cloud geometry using a scanning cloud radar, *Atmos. Meas. Tech.*, 8, 2491–2508, doi:10.5194/amt-8-2491-2015, 2015.
- 590 Fan, J., Han, B., Varble, A., Morrison, H., North, K., Kollias, P., Chen, B., Dong, X., Giangrande, S. E., Khain, A., Lin, Y., Mansell, E., Milbrandt, J. A., Stenz, R., Thompson, G., and Wang, Y.: Cloud-resolving model intercomparison of an MC3E squall line case: Part I—Convective updrafts, *J. Geophys. Res. Atmos.*, 122, 9351–9378, doi:10.1002/2017JD026622, 2017.
- Fan, J., Leung, L. R., Li, Z., Morrison, H., Chen, H., Zhou, Y., Qian, Y., and Wang, Y.: Aerosol impacts on clouds and precipitation in eastern China: Results from bin and bulk microphysics, *J. Geophys. Res.*, 117, D00K36, <https://doi.org/10.1029/2011JD016537>, 2012.
- 595 Feingold, G., Kreidenweis, S. M., Stevens, B., and Cotton, W. R.: Numerical simulations of stratocumulus processing of cloud condensation nuclei through collision-coalescence, *J. Geophys. Res.*, 101(D16), 21,391–21,402, doi:10.1029/96JD01552, 1996.
- 600 Friedrich, K. and Hagen, M.: Wind synthesis and quality control of multiple-Doppler-derived horizontal wind fields, *J. Appl. Meteor.*, 43, 38-57, doi:10.1175/1520-0450(2004)043<0038:WSAQCO>2.0.CO;2, 2004.
- Gustafson, W.I., Vogelmann, A.M., Cheng, X., Dumas, K.K., Endo, S., Johnson, K.L., Krishna, B., Li, Z., Toto, T., and Xiao, H.: Description of the LASSO Data Bundles Product. DOE Atmospheric Radiation Measurement user facility, DOE/SC-ARM-TR-216, <http://dx.doi.org/10.2172/1469590>, 2019.
- 605 Gustafson Jr., W. I., Vogelmann, A. M., Cheng, X., Endo, S., Krishna, B., Li, Z., Toto, T., Xiao, H.: Recommendations for Implementation of the LASSO Workflow, DOE/SC-ARM-17-031, doi:10.2172/1406259, 2017.
- Hogan, R. J., Jakob, C., and Illingworth, A. J.: Comparison of ECMWF Winter-Season Cloud Fraction with Radar-Derived Values. *J. Appl. Meteorol.*, 40, 513-525, doi:[http://dx.doi.org/10.1175/1520-0450\(2001\)040<0513:COEWSC>2.0.CO;2](http://dx.doi.org/10.1175/1520-0450(2001)040<0513:COEWSC>2.0.CO;2), 2001
- 610 Illingworth, A., Hogan, R., O'connor, E., Bouniol, D., Brooks, M., Delanoë, J., Donovan, D., Eastment, J., Gaussiat, N., ~~and~~ Goddard, J. W., and co-authors, CLOUDNET Cloudnet, J.: Continuous evaluation of cloud profiles in seven operational models using ground-based observations, *Bull. Amer. Meteor. Soc.*, 88(6), 883-898, doi: <https://doi.org/10.1175/BAMS-88-6-883>, 2007.
- 615 Jensen, M. P., Petersen, W. A., Bansemer, A., Bharadwaj, N., Carey, L. D., Cecil, D. J., Collis, S. M., Del Genio, A. D., Dolan, B., Gerlach, J., Giangrande, S. E., Heymsfield, A., Heymsfield, G., Kollias, P., Lang, T. J., Nesbitt, S. W., Neumann, A.,

- Poellot, M., Rutledge, S. A., Schwaller, M., Tokay, A., Williams, C. R., Wolff, D. B., Xie, S., and Zipser, E. J.: The Midlatitude Continental Convective Clouds Experiment (MC3E), *Bull. Amer. Meteor. Soc.*, 1667-1686, doi: 10.1175/BAMS-D-14-00228.1, 2016.
- 620 [Jiang, Z., Kumjian, M.R., Schrom, R.S., Giammanco, I., Brown-Giammanco, T., Estes, H., Maiden, R., and Heymsfield, A.J.: Comparisons of Electromagnetic Scattering Properties of Real Hailstones and Spheroids. *J. Appl. Meteor. Climatol.*, 58, 93–112, <https://doi.org/10.1175/JAMC-D-17-0344.1>, 2019.](#)
- Jorgensen, D. P. and LeMone, M. A.: Vertically velocity characteristics of oceanic convection, *J. Atmos. Sci.*, 46, 621–640, doi: 10.1175/1520-0469(1989)046<0621:VVC0OC>2.0.CO;2, 1989.
- 625 [Kneifel, S., Dias Neto, J., Ori, D., Moisseev, D., Tyynelä, J., Adams, I. S., Kuo, K.-S., Bennartz, R., Berne, A., Clothiaux, E. E., Eriksson, P., Geer, A. J., Homeyager, R., Leinonen, J., and Westbrook, C. D.: The first international summer snowfall workshop: Scattering properties of realistic frozen hydrometeors from simulations and observations, as well as defining a new standard for scattering databases. *Bulletin of the American Meteorological Society*. doi:10.1175/BAMS-D-17-0208.1, 2018](#)
- 630 Kneifel, S., Lerber, A., Tiira, J., Moisseev, D., Kollias, P., [and](#) Leinonen, J.: Observed relations between snowfall microphysics and triple-frequency radar measurements. *Journal of Geophysical Research*, 120, 6034–6055, doi:10.1002/2015JD023156, 2015.
- Kneifel, S., Kollias, P., Battaglia, A., Leinonen, J., Maahn, M., Kalesse, H., and Tridon, F.: First observations of triple frequency radar Doppler spectra in snowfall: Interpretation and applications. *Geophysical Research Letters*, 43, 2225–2233, doi:10.1002/2015GL067618, 2016.
- 635 Kollias, P., McLaughlin, D. J., Frasier, S., Oue, M., Luke, E., and Sneddon, A.: Advances and applications in low-power phased array X-band weather radars. Proc. 2018 IEEE Radar Conference, Oklahoma City, OK, USA, doi: 10.1109/RADAR.2018.8378762, 2018.
- Kollias, P., Miller, M. A., Johnson, K. L., Jensen, M. P., and Troyan, D. T.: Cloud, thermodynamic, and precipitation observations in West Africa during 2006. *J. Geophys. Res. Atmos.*, 114, D00E08, doi:10.1029/2008JD010641, 2009.
- 640 Kollias, P. and Tanelli, S., Battaglia, A., Tatarevic, A.: Evaluation of EarthCARE cloud profiling radar Doppler velocity measurements in particle sedimentation regimes. *J. Atmos. Oceanic Technol.*, 31, 366-386, doi: 10.1175/JTECH-D-11-00202.1, 2014.
- Lamer, K., Fridlind, A. M., Ackerman, A. S., Kollias, P., Clothiaux, E. E., and Kelley, M.: (GO)2-SIM: a GCM-oriented ground-observation forward-simulator framework for objective evaluation of cloud and precipitation phase. *Geosci. Model Dev.*, 11, 4195-4214, <https://doi.org/10.5194/gmd-11-4195-2018>, 2018.
- 645 Lamer, K. and Kollias, P.: Observations of fair-weather cumuli over land: Dynamical factors controlling cloud size and cover, *Geophys. Res. Lett.*, 42, 8693-8701, doi: 10.1002/2015GL064534, 2015.
- Lamer, K., Tatarevic, A., Jo, I., and Kollias P.: Evaluation of gridded Scanning ARM Cloud Radar reflectivity observations and vertical Doppler velocity retrievals, *Atmos. Meas. Tech.*, 7, 1089-1103, doi:10.5194/amt-7-1089-2014, 2013.
- 650 Larson, V. E., Wood, R., Field, P. R., Golaz, J.-C., Vonder Haar, T. H., and Cotton W. R.: Small-scale and mesoscale variability of scalars in cloudy boundary layers: One-dimensional probability density functions., *J. Atmos. Sci.*, 58, 1978-1994, doi: 10.1175/1520-0469(2001)058<1978:SSAMVO>2.0.CO;2, 2001.
- [Leinonen, J., and Moisseev, D.: What do triple-frequency radar signatures reveal about aggregate snowflakes? *Journal of Geophysical Research: Atmospheres*, 120, 229–239. doi:10.1002/2014JD022072, 2015.](#)
- 655 [Leinonen, J., and Szyrmer, W: Radar signatures of snowflake riming: A modeling study. *Earth and Space Science*, 2\(8\), 346–358. doi:10.1002/2015EA000102, 2015](#)
- Löhnert, U., Schween, J. H., Acquistapace, C., Ebell, K., Maahn, M., Barrera-Verdejo, M., Hirsikko, A., Bohn, B., Knaps, A., O’connor, E., Simmer, C., Wahner, A., and Crewell, S.: JOYCE: Jülich Observatory for Cloud Evolution, *Bull. Amer. Meteor. Soc.*, 96, 1157–1174, doi:10.1175/BAMS-D-14-00105.1, 2015.

- 660 [Lu, Y., Jiang, Z., Aydin, K., Verlinde, J., Clothiaux, E. E., and Botta, G.: A polarimetric scattering database for non-spherical ice particles at microwave wavelengths. *Atmospheric Measurement Techniques*, 9\(10\), 5119–5134. <https://doi.org/10.5194/amt-9-5119-2016>, 2016](https://doi.org/10.5194/amt-9-5119-2016)
- Luke, E., Kollias, P., and Shupe, M.: Detection of supercooled liquid in mixed-phase clouds using radar Doppler spectra. *J. Geophys. Res. Atmos.*, 115, D19201, doi:10.1029/2009JD012884, 2010.
- 665 Mather, J. H., Turner, D. D., and Ackerman, T. P.: Scientific maturation of the ARM Program. The Atmospheric Radiation Measurement (ARM) Program: The First 20 Years, Meteor. Monogr., No. 57, *Amer. Meteor. Soc.*, doi: 10.1175/AMSMONOGRAPHS-D-15-0053.1, 2016.
- Matrosov, S. Y., Schmitt, C. G., Maahn, M., and de Boer, G.: Atmospheric ice particle shape estimates from polarimetric radar measurements and in situ observations. *J. Atmos. Oceanic Technol.*, 34, 2569–2587, doi: <https://doi.org/10.1175/JTECH-D-17-0111.1>, 2017.
- 670 [Matsui, T., Dolan, B., Rutledge, S. A., Tao, W.-K., Iguchi, T., Barnum, J., and Lang, S. E.: POLARRIS: A POLARimetric Radar Retrieval and Instrument Simulator. *Journal of Geophysical Research: Atmospheres*, 124, 4634–4657. Doi: <https://doi.org/10.1029/2018JD028317>, 2019](https://doi.org/10.1029/2018JD028317)
- 675 [Maxwell Garnet, J. C.: Colours in Metal Glasses and in Metallic Films. *Philosophical Transactions of the Royal Society of London. Series A, Containing Papers of a Mathematical or Physical Character*, 203, pp. 385–420. JSTOR, \[www.jstor.org/stable/90866\]\(http://www.jstor.org/stable/90866\), 1904](http://www.jstor.org/stable/90866)
- Milbrandt, J. A., and Yau, M. K.: A multimoment bulk microphysics parameterization. Part I: Analysis of the role of the spectral shape parameter. *J. Atmos. Sci.*, 62, 3051–3064, <https://doi.org/10.1175/JAS3534.1>, 2005a.
- Milbrandt, J. A., and Yau, M. K.: A multimoment bulk microphysics parameterization. Part II: A proposed three-moment closure and scheme description. *J. Atmos. Sci.*, 62, 3065–3081, <https://doi.org/10.1175/JAS3535.1>, 2005b.
- 680 Mishchenko, M. I. and Travis, L. D.: Capabilities and limitations of a current FORTRAN implementation of the T-matrix method for randomly oriented, rotationally symmetric scatterers, *J. Quant. Spectrosc. Radiat. Transfer*, 60, 309–324, [https://doi.org/10.1016/S0022-4073\(98\)00008-9](https://doi.org/10.1016/S0022-4073(98)00008-9), 1998.
- Mishchenko, M. I.: Calculation of the amplitude matrix for a nonspherical particle in a fixed orientation. *Appl. Opt.*, 39, 1026–1031, <https://doi.org/10.1364/AO.39.001026>, 2000.
- 685 Morrison, H., Curry, J. A., and Khvorostyanov, V. I.: A new double-moment microphysics parameterization for application in cloud and climate models. Part I: Description. *J. Atmos. Sci.*, 62, 1665–1677, <https://doi.org/10.1175/JAS3446.1>, 2005.
- Morrison, H. and Milbrandt, J. A.: Parameterization of cloud microphysics based on the prediction of bulk Ice particle properties. Part I: Scheme description and idealized tests. *J. Atmos. Sci.*, 72, 287–311, <https://doi.org/10.1175/JAS-D-14-0065.1>, 2015.
- 690 North, K. W., Oue, M., Kollias, P., Giangrande, S. E., Collis, S. M., and Potvin, C. K.: Vertical air motion retrievals in deep convective clouds using the ARM scanning radar network in Oklahoma during MC3E, *Atmos. Meas. Tech.* 10, 1 – 14, doi: 10.5194/amt-10-2785-2017, 2017.
- O'Connor, E. J., Illingworth, A. J., and Hogan, R. J.: A technique for autocalibration of cloud lidar, *J. Atmos. Ocean. Tech.*, 21, 777–786, doi: 10.1175/1520-0426(2004)021<0777:ATFAOC>2.0.CO;2, 2004.
- 695 Oue, M., Inagaki, K., Shinoda, T., Ohigashi, T., Kouketsu, T., Kato, M., Tsuboki, K., Uyeda H.: Polarimetric Doppler radar analysis of organization of a stationary rainband with changing orientations in July 2010, *J. Meteorol. Soc. Jpn.*, 22, 457–481, doi: 10.2151/jmsj.2014-503, 2014.
- Oue, M., Kollias, P., North, K. W., Tatarevic, A., Endo, S., Vogelmann, A. M., and Gustafson Jr., W. I.: Estimation of cloud fraction profile in shallow convection using a scanning cloud radar. *Geophys. Res. Lett.*, 43, 10998–11006, doi: 10.1002/2016GL070776, 2016.
- 700 Oue, M., Kollias, P., Shapiro, A., Tatarevic, A., and Matsui, T.: Investigation of observational error sources in multi-Doppler-radar three-dimensional variational vertical air motion retrievals, *Atmos. Meas. Tech.*, 12, 1999–2018, <https://doi.org/10.5194/amt-12-1999-2019>, 2019a.

- 705 [Oue, M., Matsui, T., and Kollias, P.: Configuration files and input data used for radar simulations described in "The Cloud Resolving Model Radar Simulator \(CR-SIM\) Version 3.2: Description and Applications of a Virtual Observatory" SoMAS Research Data. 3. <https://commons.library.stonybrook.edu/somasdata/3>, 2019b.](https://commons.library.stonybrook.edu/somasdata/3)
- Potvin, C. K., Wicker, L. J., and Shapiro A.: Assessing errors in variational dual-Doppler wind syntheses of supercell thunderstorms observed by storm-scale mobile radars, *J. Atmos. Ocean. Tech.*, 29, 1009–1025, doi: 10.1175/JTECH-D-11-00177.1, 2012.
- 710 [Ray, P. S.: Broadband complex refractive indices of ice and water. *Applied optics*, 11\(8\), 1836-1844, 1972.](https://doi.org/10.1080/00036817208839000)
- Rémillard, J., Kollias, P., and Szyrmer, W.: Radar-radiometer retrievals of cloud number concentration and dispersion parameter in non drizzling marine stratocumulus, *Atmos. Meas. Tech.*, 6, 1817-1828, doi:10.5194/amt-6-1817-2013, 2013
- Ryzhkov, A. V.: Interpretation of polarimetric radar covariance matrix for meteorological scatterers: Theoretical analysis. *J. Atmos. Oceanic Technol.*, 18, 315–328, [https://doi.org/10.1175/1520-0426\(2001\)018<0315:IOPRCM>2.0.CO;2](https://doi.org/10.1175/1520-0426(2001)018<0315:IOPRCM>2.0.CO;2), 2001.
- 715 Ryzhkov A. V., Pinsky, M., Pokrovsky, A., and Khain, A.: Polarimetric Radar Observation Operator for a Cloud Model with Spectral Microphysics. *J. Appl. Meteor. Climatol.*, 50, 873–894, <https://doi.org/10.1175/2010JAMC2363.1>, 2011.
- Seifert, A.: On the parameterization of evaporation of raindrops as simulated by a one-dimensional rainshaft model, *J. Atmos. Sci.*, 65, 3608-3619, <https://doi.org/10.1175/2008JAS2586.1>, 2008.
- 720 Seifert, A. and Beheng, K. D.: A two-moment cloud microphysics parameterization for mixed-phase clouds. Part 1: Model description. *Meteorol. Atmos. Phys.*, 92, 45-66, <https://doi.org/10.1007/s00703-005-0112-4>, 2006.
- [Shapiro, A., Willingham, K. M., and Potvin, C. K.: Spatially variable advection correction of radar data. Part I: Theoretical considerations, *J. Atmos. Sci.*, 67, 3445-3456, doi: 10.1175/2010JAS3465.1, 2010a.](https://doi.org/10.1175/2010JAS3465.1)
- 725 Shupe, M. D.: A ground-based multiple remote-sensor cloud phase classifier, *Geophys. Res. Lett.*, 34, L22809, doi:10.1029/2007GL031008, 2007.
- Skamarock, W. C., Klemp, J. B., Dudhia, J., Gill, D. O., Barker, D. M., Duda, M. G., Wang, W., and Powers, J. G: A description of the advanced research WRF version 3. NCAR Technical Note, NCAR/TN-475+STR, National Center for Atmospheric Research, 113 pp, <https://doi.org/10.5065/D68S4MVH>, 2008.
- Snyder, J. C., Bluestein, H. B., Dawson II, D. T., and Jung, Y.: Simulations of polarimetric, X-band radar signatures in supercells. Part I: Description of experiment and simulated ρ_{hv} rings. *J. Appl. Meteorol. Climatol.*, 56, 1977 – 1999, doi: 10.1175/JAMC-D-16-0138.1, 2017a.
- 730 Snyder, J. C., Bluestein, H. B., Dawson II, D. T., and Jung, Y.: Simulations of polarimetric, X-band radar signatures in supercells. Part II: Z_{DR} columns and rings and K_{DP} columns. *J. Appl. Meteorol. Climatol.*, 56, 1977 – 1999, doi: 10.1175/JAMC-D-16-0139.1, 2017b.
- 735 Spinhirne, J. D.: Micro Pulse Lidar. *IEEE Transactions on Geoscience and Remote Sensing*, 31, 48–55, 1993.
- Stevens, B., Farrell, D., Hirsch, L., Jansen, F., Nuijens, L., Serikov, I., Brüggmann, B., Forde, M., Linne, H., Lonitz, K., and Prospero, J. M.: The Barbados cloud Observatory: Anchoring investigations of clouds and circulation on the edge of the ITCZ, *Bull. Amer. Meteor. Soc.*, 97, 787-801, doi: 10.1175/BAMS-D-14-00247.1, 2016.
- 740 Szyrmer, W., Tatarevic, A., and Kollias, P.: Ice clouds microphysical retrieval using 94-GHz Doppler radar observations: Basic relations within the retrieval framework, *J. Geophys. Res. Atmos.*, 117, D14203, doi:10.1029/2011JD016675, 2012
- Szyrmer, W. and Zawadzki, I.: *J. Atmos. Sci.*, 71,1171–1186, Snow Studies. Part IV: Ensemble Retrieval of Snow Microphysics from Dual-Wavelength Vertically Pointing Radars, *J. Atmos. Sci.*, 71, 1171–1186, <https://journals.ametsoc.org/doi/abs/10.1175/JAS-D-12-0286.1>, 2014.
- 745 Tatarevic, A., Kollias, P., Oue, M., Wang, D., and Yu, K.: User’s Guide CR-SIM SOFTWARE v 3.1, Brookhaven National Laboratory - Stony Brook University - McGill University Radar Science Group, 2018. [Available at <https://www.bnl.gov/CMAS/cr-sim.php>; <https://you.stonybrook.edu/radar/research/radar-simulators/>.]

- Thompson, G., Field, P. R., Rasmussen, R. M., and Hall, W. D.: Explicit forecasts of winter precipitation using an improved bulk microphysics scheme. Part II: Implementation of a new snow parameterization. *Mon. Wea. Rev.*, 136, 5095–5155, 2008.
- 750 Turner, D.D. and Ellingson, R.G.: Introduction. *Meteorological Monographs*, 57, v–x, <https://doi.org/10.1175/AMSMONOGRAPHIS-D-16-0001.1>, 2016.
- Tzivion, S., Feingold, G., and Levin, Z.: An efficient numerical solution to the stochastic collection equation, *J. Atmos. Sci.*, 44, 3139–3149, doi: 10.1175/1520-0469(1987)044<3139:AENSTT>2.0.CO;2, 1987.
- 755 Yurkin, M. A., and A. G. Hoekstra, 2011: The discrete-dipole-approximation code ADDA: Capabilities and known limitations. *J. Quant. Spectrosc. Radiat. Transfer*, 112, 2234–2247, doi: 10.1016/j.jqsrt.2011.01.031.
- Von Lerber, A., Moisseev, D., Bliven, L., Petersen, W., Harri, A., and Chandrasekar, V.: Microphysical properties of snow and their link to $Z_e - S$ relations during BAECC 2014. *J. Appl. Meteorol.*, 56, 1561 – 1582, 2017.
- van Stratum, B. J. H., Vilá-Guerau de Arellano, J., van Heerwaarden, C. C., and Ouwersloot, H. G.: Subcloud-layer feedbacks driven by the mass flux of shallow cumulus convection over land. *J. Atmos. Sci.*, 71, 881–895, doi: 10.1175/JAS-D-13-0192.1, 2014.
- 760 Varble, A., Zipser, E. J., Fridlind, A. M., Zhu, P., Ackerman, A. S., Chaboureau, J.-P., Collis, S., Fan, J., Hill, A., and Shipway, B.: Evaluation of cloud-resolving and limited area model intercomparison simulations using TWP-ICE observations: 1. Deep convective updraft properties, *J. Geophys. Res. Atmos.*, 119, 13,891–13,918, doi:10.1002/2013JD021371, 2014.
- Wood, R., and Field, P. R.: The distribution of cloud horizontal sizes. *J. Clim.*, 24, 4800–4816, doi: 10.1175/2011JCLI4056.1, 2011.
- 765 Zhang, D., Wang, W., Heymsfield, A., Fan, J., and Luo, T.: Ice concentration retrieval in stratiform mixed-phase clouds using cloud radar reflectivity measurements and 1d ice growth model simulations. *J. Atmos. Sci.*, 71, 3613–3635, doi:10.1175/JAS-D-13-0354.1, 2014.
- Zhang, Y., Xie, S., Klein, S. A., Marchand, R., Kollias, P., Clothiaux, E. E., Lin, W., Johnson, K., Swales, D., Bodas-Salcedo, A., Tang, S., Haynes, J. M., Collis, S., Jensen, M., Bharadwaj, N., Hardin, J., and Isom, B.: The ARM cloud radar simulator for global climate models., *Bull. American Meteorol. Soc.*, 99, 21 – 26, doi: 10.1175/BAMS-D-16-0258.1, 2018.
- 770 [Wurman, J., The DOW mobile multiple-Doppler network. Preprints, 30th Int. Conf. on Radar Meteorology, Munich, Germany, Amer. Meteor. Soc., 95–97, 2001.](#)

Table 1. The minimum and maximum sizes and sizebin spacing of simulated particles for each hydrometeor category from the bulk microphysics schemes except the P3 scheme. 'The Particle size' here refers to the particle maximum dimension.

<u>Category</u>	<u>Minimum size [μm]</u>	<u>Maximum size [μm]</u>	<u>SizeBin spacing [μm]</u>
<u>Cloud</u>	<u>1</u>	<u>250</u>	<u>1</u>
<u>Drizzle</u>	<u>1</u>	<u>250</u>	<u>1</u>
<u>Rain</u>	<u>100</u>	<u>9000</u>	<u>20</u>
<u>Ice</u>	<u>1</u>	<u>1496</u>	<u>5</u>
<u>Snow, aggregates</u>	<u>100</u>	<u>50000</u>	<u>100</u>
<u>Graupel</u>	<u>5</u>	<u>50005</u>	<u>100</u>
<u>Hail</u>	<u>5</u>	<u>50005</u>	<u>100</u>

780

Table 24. Incorporated microphysics schemes and corresponding CRMs.

CRM	Microphysics scheme (M=moment)
Weather Research and Forecasting Model (WRF)	Morrison 2-M scheme (Morrison et al. 2005)
	Milbrandt and Yau multi-M scheme (Milbrandt and Yau 2005a, 2005b)
	Thompson 1- and 2-M scheme (Thompson et al. 2008)
	Predicted particle properties (P3) scheme (Morrison and Milbrandt 2015)
	Spectral bin microphysics (Fan et al. 2012)
ICOsahedral Non-hydrostatic general circulation model (ICON)	Seifert and Beheng 2-M scheme (Seifert and Beheng 2006; Seifert 2008)
Regional Atmospheric Modeling System (RAMS)	2-M scheme (Cotton et al., 2003)
System for Atmospheric Modeling (SAM)	Tel Aviv University 2-M bin microphysics (Tzivion et al. 1987; Feingold et al. 1996)
	Morrison 2-M scheme (Morrison et al. 2005)

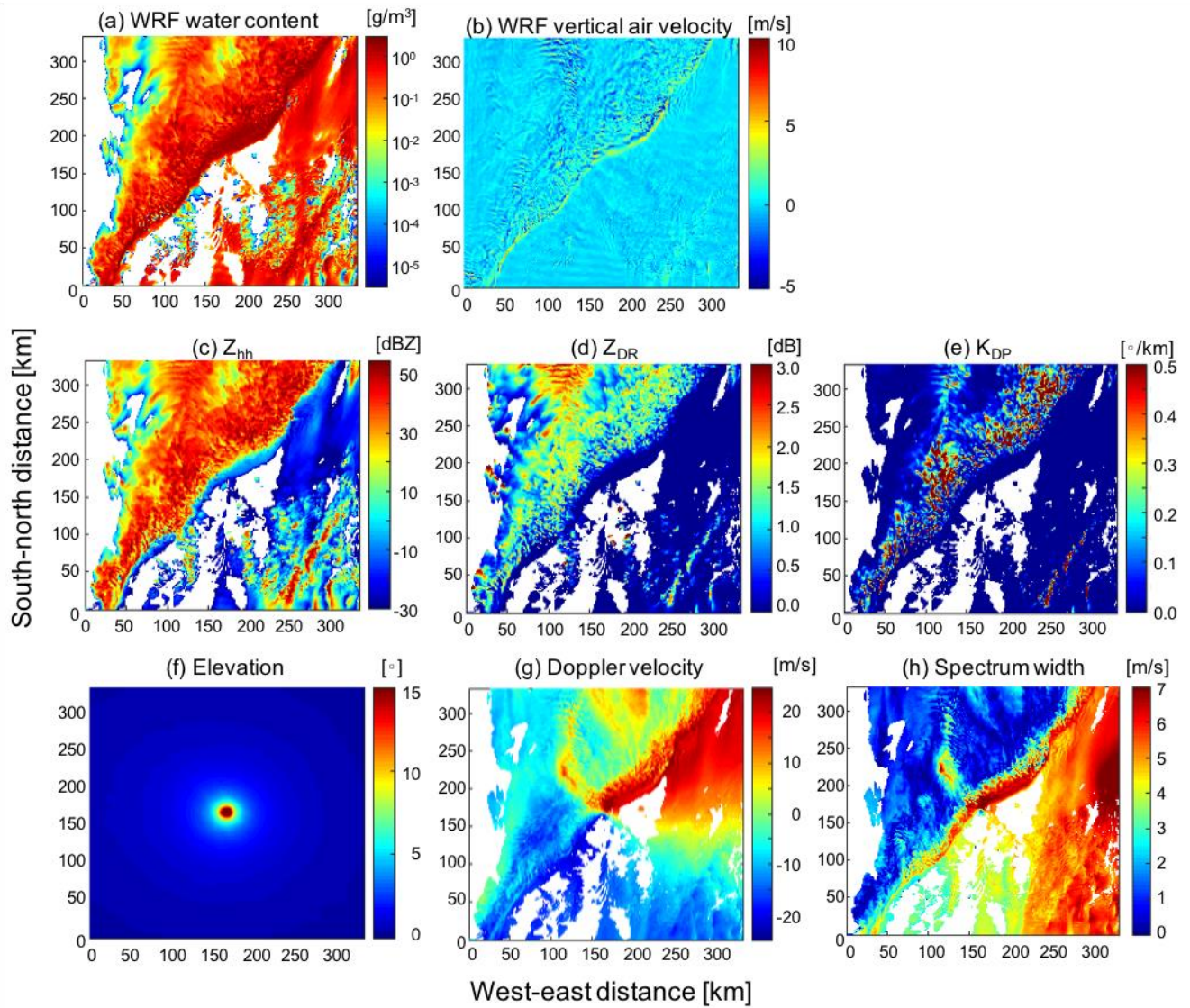
785

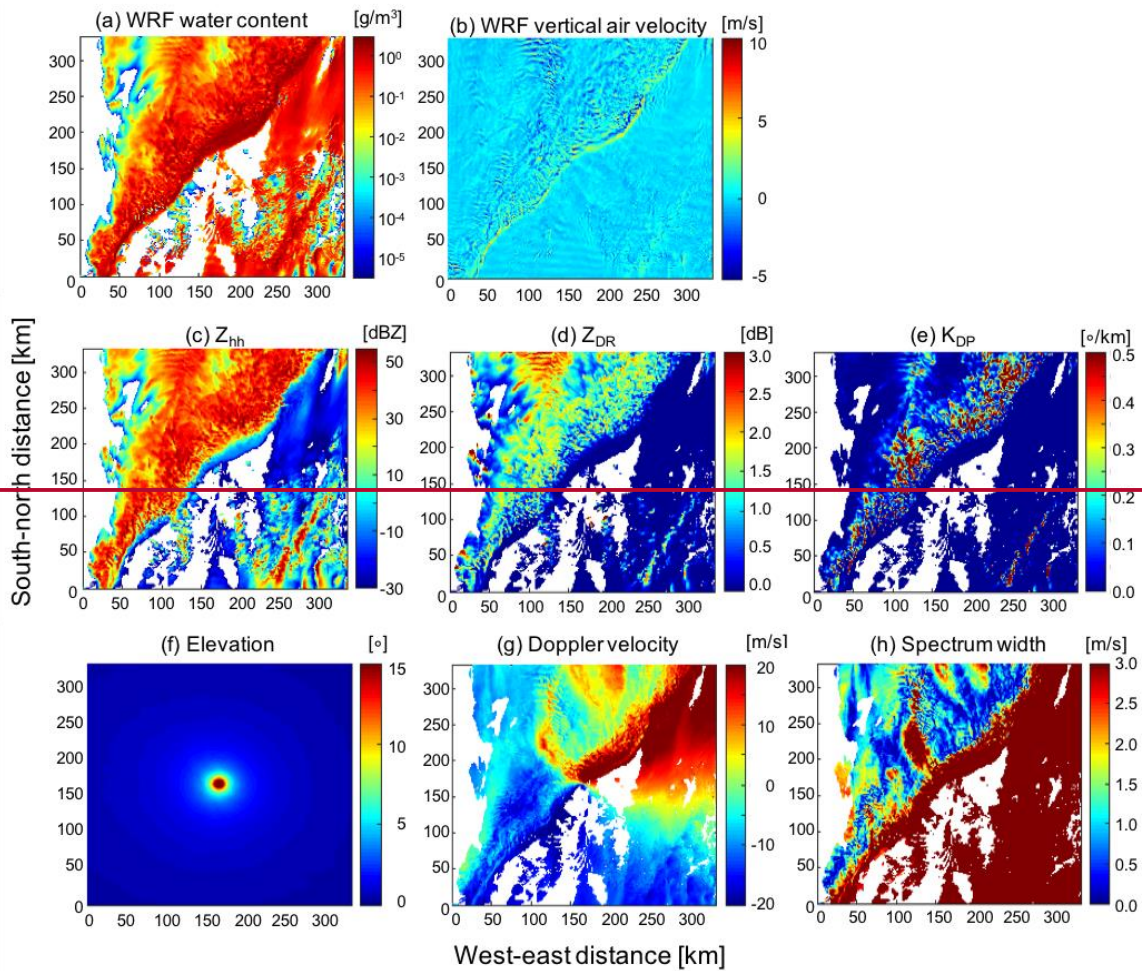
Table 23. Computed radar variables. Units of each the variables stored in output files are represented provided in square brackets.

Variable	Description
Z_{hh}	Radar reflectivity factor at horizontal polarization [dBZ]
Z_{vv}	Radar reflectivity factor at vertical polarization [dBZ]
Z_{vh}	Cross-polarization radar reflectivity factor [dBZ]
Z_{DR}	Differential reflectivity, defined as the ratio between the fraction of horizontally polarized backscattering and vertically polarized backscattering [dB]
LDR_h	Linear depolarization ratio, defined as the ratio of the power backscattered at vertical polarization to the power backscattered at horizontal polarization for a horizontally polarized field [dB]
K_{DP}	Specific differential phase, the backward propagation phase difference between the horizontally and vertically polarized waves at a specific distance [$^{\circ} \text{ km}^{-1}$]
δ	Differential backscatter phase, defined as the difference between the phases of horizontally and vertical polarized components of the wave caused by backscattering from the objects in the radar resolution volume, computed based on Trömel et al (2013) [$^{\circ}$]
A_h	Specific attenuation at horizontal polarization, or for horizontally polarized waves, represented by forward scattering amplitudes [dB km^{-1}]
A_v	Specific attenuation at vertical polarization, or for vertically polarized waves, represented by forward scattering amplitudes [dB km^{-1}]
A_{DP}	Specific differential attenuation, defined as the difference between the specific attenuations for horizontally and vertically polarized waves [dB km^{-1}]
V_D	Mean radial Doppler velocity (positive away from the radar) [m s^{-1}]
$V_{D_{90}}$	Mean vertical Doppler velocity (positive upward) [m s^{-1}]
SW_{TOT}	Spectrum width, including contribution of four major spectral broadening mechanisms (Doviak and Zrníc, 2006): 1) different hydrometeor terminal velocity of different sizes SW_H , 2) turbulence, 3) mean wind shear contribution, and 4) cross wind contribution. Antenna motion and contributions due to variation of orientation and vibrations of hydrometeor are not considered. [m s^{-1}]
$SW_{H_{90}}$	Spectrum width due to different hydrometeor terminal velocity of different sizes in vertical, such that $SW_{H_{90}} = SW_H$ ($\theta=90^{\circ}$), where θ is the elevation angle measured from horizontal [m s^{-1}]
V_{RW}	Reflectivity weighted velocity (positive downward) [m s^{-1}]
Z_{MIN}	Radar minimum detectable reflectivity [dBZ]
Spectra_ Z_{hh}	Radar Doppler spectra at horizontal polarization [m s^{-1} dB $^{-1}$]
<u>Spectra_ Z_{vv}</u>	<u>Radar Doppler spectra at vertical polarization [m s^{-1} dB$^{-1}$]</u>
<u>Spectra_ Z_{vh}</u>	<u>Cross-polarization radar Doppler spectra [m s^{-1} dB$^{-1}$]</u>

Table 34. Computed lidar variables

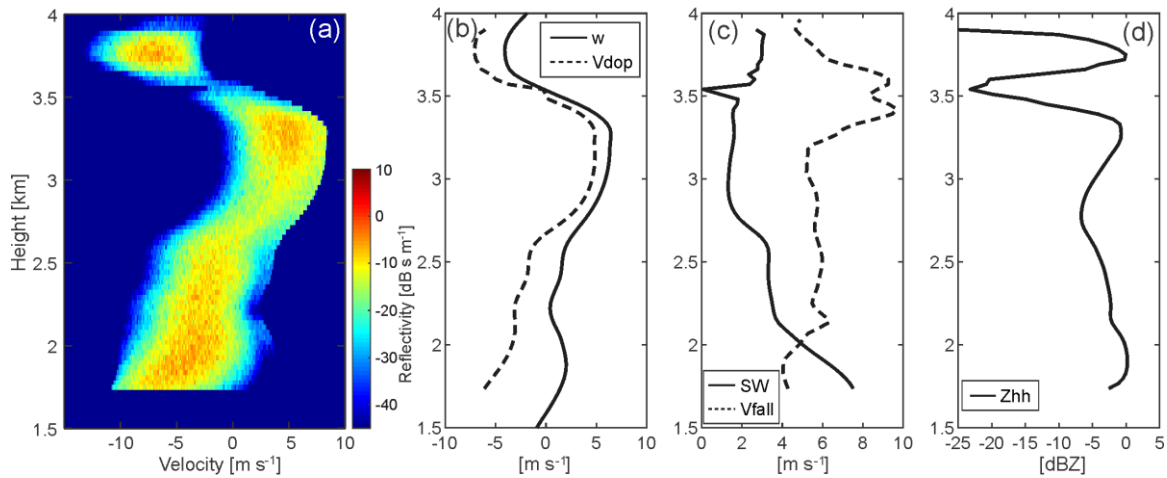
Variable	Description
$\beta_{hydro}, \beta_{aero}, \beta_{mol}$	Backscatter [$\text{sr}^{-1} \text{m}^{-1}$] for cloud droplets and cloud ice (β_{hydro}), aerosols (β_{aero}), and air molecules (β_{mol})
$\beta_{hydro_atten}, \beta_{aero_atten}, \beta_{mol_atten}$	Attenuated backscatter [$\text{sr}^{-1} \text{m}^{-1}$] for cloud droplets and cloud ice (β_{hydro_atten}), aerosols (β_{aero_atten}), and air molecules (β_{mol_atten})
$\alpha_{ext_hydro}, \alpha_{ext_aero}$	Extinction coefficient [m^{-1}] for cloud droplets and cloud ice (α_{ext_hydro}) and aerosols (α_{ext_aero})
β_{total}	Total backscatter [$\text{sr}^{-1} \text{m}^{-1}$], defined as $\beta_{total} = \beta_{hydro} + \beta_{aero} + \beta_{mol}$
β_{total_atten}	Attenuated total backscatter [$\text{sr}^{-1} \text{m}^{-1}$], defined as $\beta_{total_atten} = \beta_{hydro_atten} + \beta_{aero_atten} + \beta_{mol_atten}$
S	Lidar ratio, defined as $S = \alpha_{ext_hydro} / \beta_{hydro}$





800

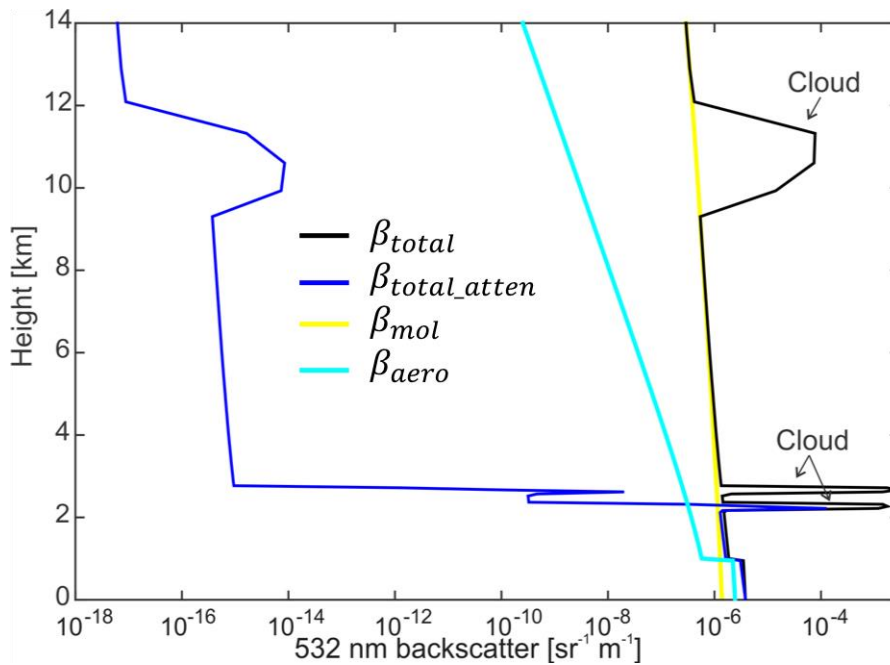
Figure 1: Radar observables produced by CR-SIM for a mesoscale convective system. The system was simulated using WRF with the Morrison 2-moment microphysics scheme at 1.8 km altitude. Shown are horizontal cross sections of (a) total hydrometeor content and (b) vertical air velocity from the WRF simulation. CR-SIM produces the following parameters for a scanning S-band (3 GHz) radar located at the center of the domain: (c) Z_{hh} , (d) Z_{DR} , (e) K_{DP} , (f) radar antenna elevation angle, (g) Doppler velocity, and (h) spectrum width at 12:18:00 UTC.



805

Figure 2: CR-SIM examples of radar observables for a shallow convection LASSO case from a WRF simulation coupled with the Thompson microphysics scheme. Shown are (a) simulated radar Doppler spectra, (b) model vertical velocity (w , solid line) and simulated mean Doppler velocity (V_{dop} , dashed line), (c) simulated spectrum width (SW , solid line) and simulated reflectivity-weighted velocity (V_{fall} , dashed line), and (d) simulated total reflectivity (Z_{hh}) at S band (3 GHz). In (a) and (b), a positive sign indicates upward motion, and in (c), a positive sign indicates downward motion (fall speed).

810



815

Figure 3: Lidar observables from CR-SIM for a cumulus case from LASSO using WRF with the Morrison 2-moment microphysics scheme. Example of simulated vertical profiles are shown for β_{total} , β_{total_atten} , β_{mol} , and β_{aero} at a wavelength of 532 nm.

820

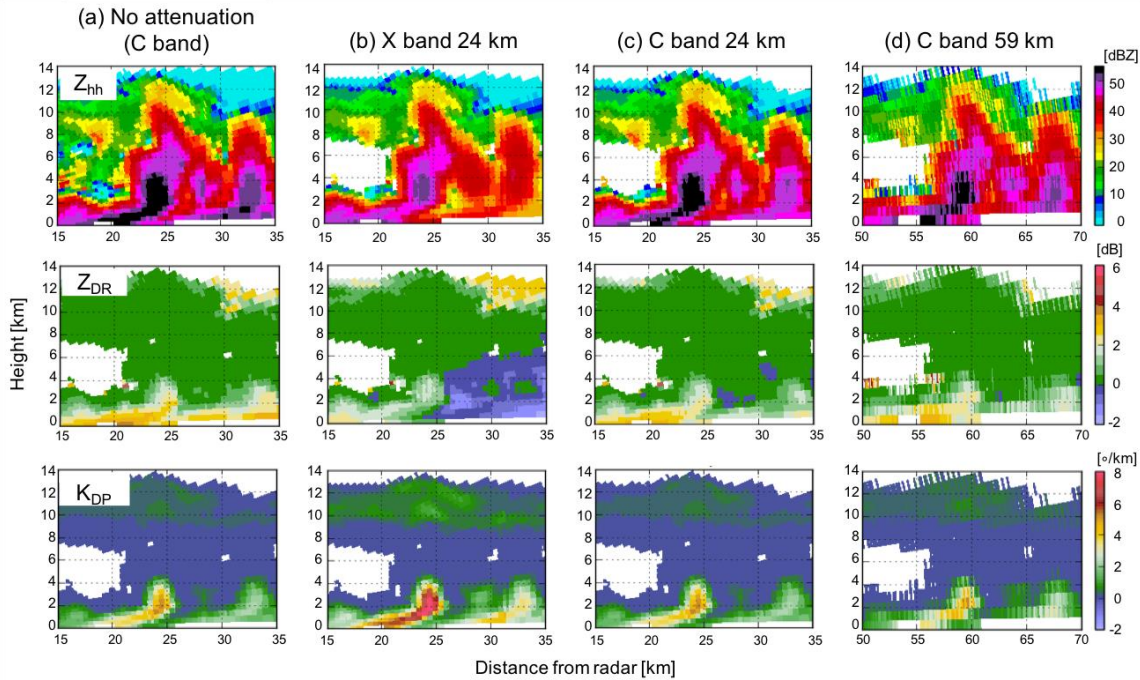


Figure 4: Examples of C- and X-band (5.5 and 9 GHz, respectively) RHI scans with a beamwidth of 1° produced using CR-SIM for a convective cell in a mesoscale convective system (MCS). The simulation uses WRF with the Morrison double moment microphysics scheme for an MCS on May, 20, 2011 during MC3E. Shown are variables at X- and C-band frequencies 15-35 km from the radar as a function of height at 12:18:00 UTC: (top row) Z_{hh} , (middle row) Z_{DR} , and (bottom row) K_{DP} . The figure shows (a) C-band variables without attenuation, (b) X-band variables with attenuation from a radar 24 km from the convective cell, (c) C-band variables with attenuation from a radar 24 km away, and (d) C-band variables from a radar located 59 km away with attenuation.

825

830

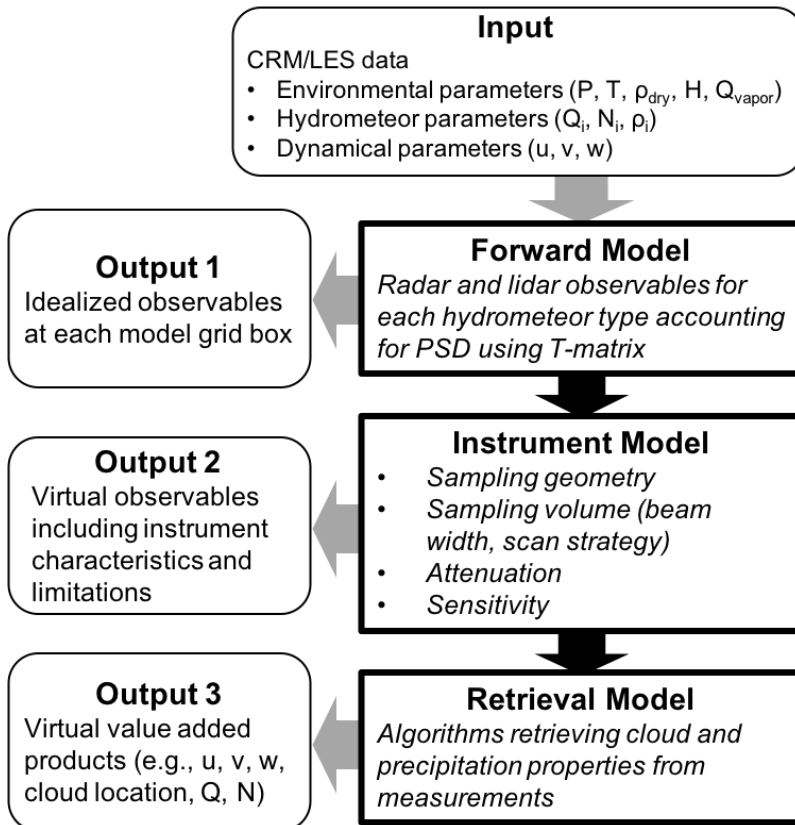
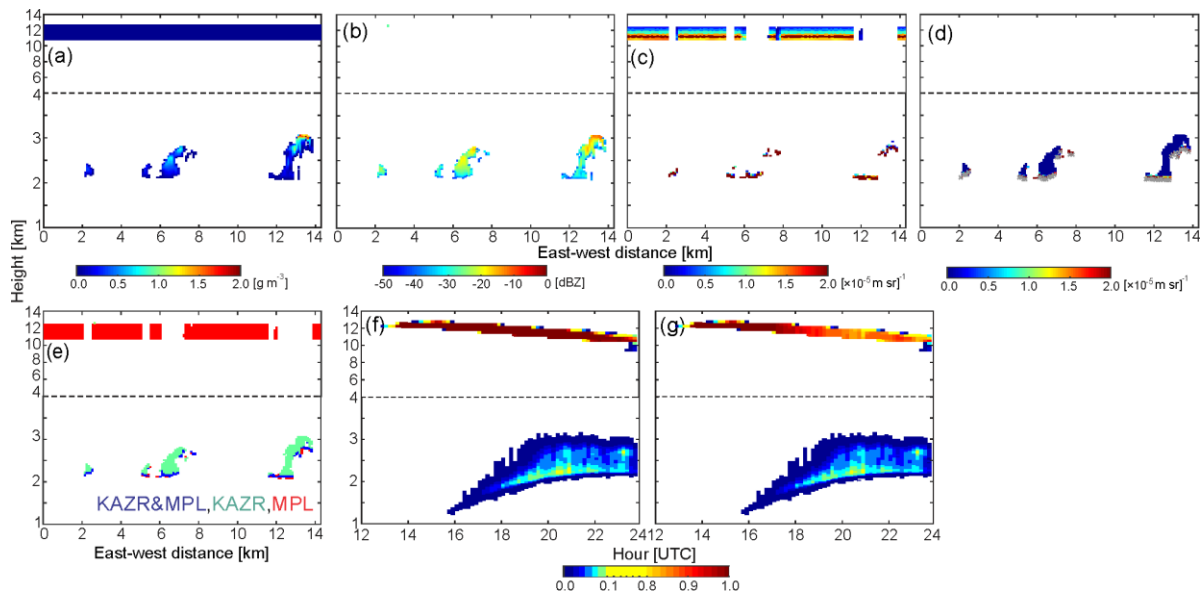


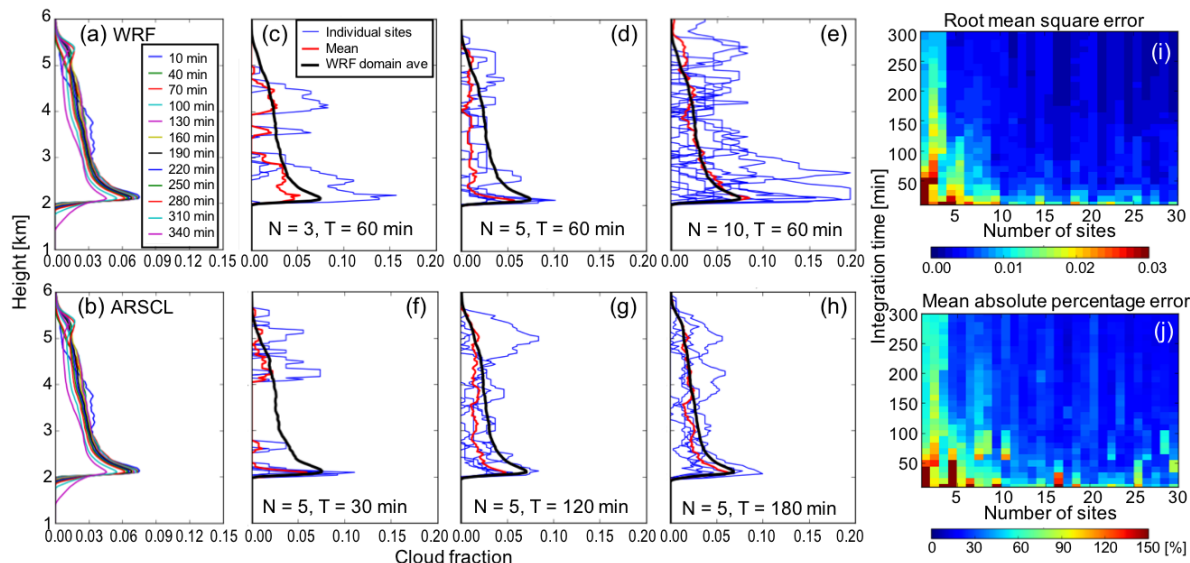
Figure 5: Diagram for CR-SIM and its applications. The diagram indicates the CR-SIM input and the different levels of output for the forward model, instrument model, and retrieval model.

835

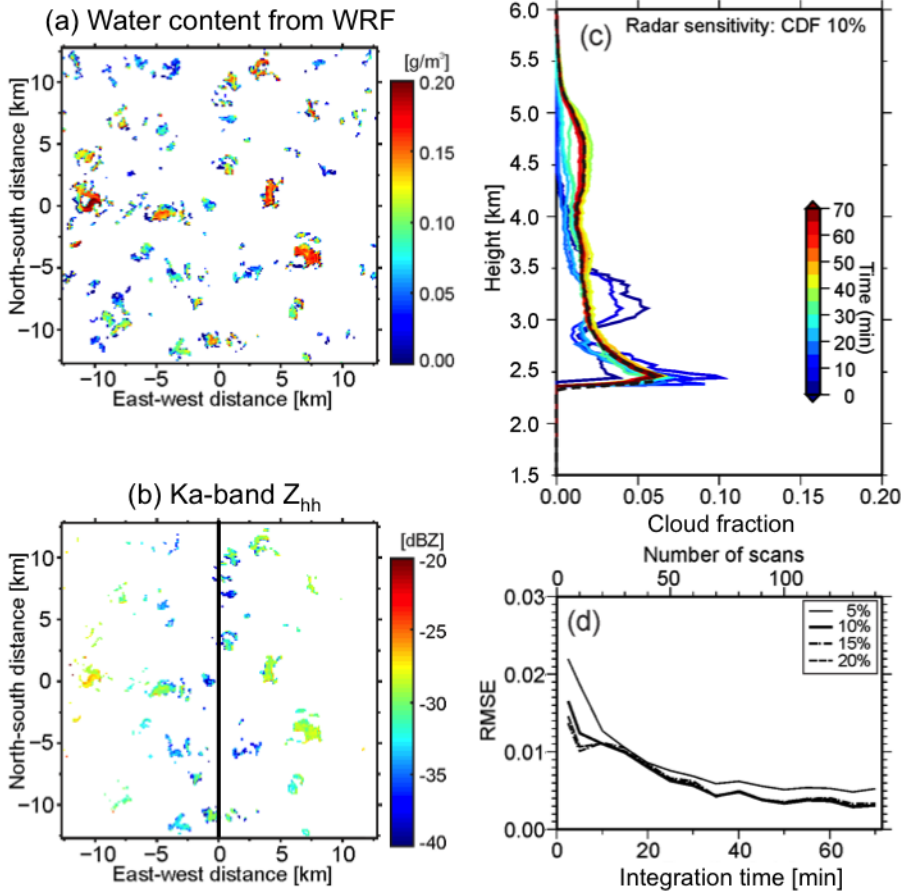
840



845
Figure 6: Simulated vertically pointing radar and lidar measurements and the ARSCL product for a shallow convection case on June 27, 2015. (a-e) Vertical cross sections of (a) water content from the WRF model, (b) Ka-band (35 GHz) radar reflectivity accounting for radar sensitivity and attenuation, (c) MPL attenuated backscatter, (d) ceilometer backscatter (color-shadebar) and first cloud base (gray dots), and (e) the ARSCL cloud mask. (f,g) Height-versus-time cross sections of domain-averaged cloud fraction from (f) WRF water content $> 0.001 \text{ g m}^{-3}$ and (g) the simulated ARSCL product.



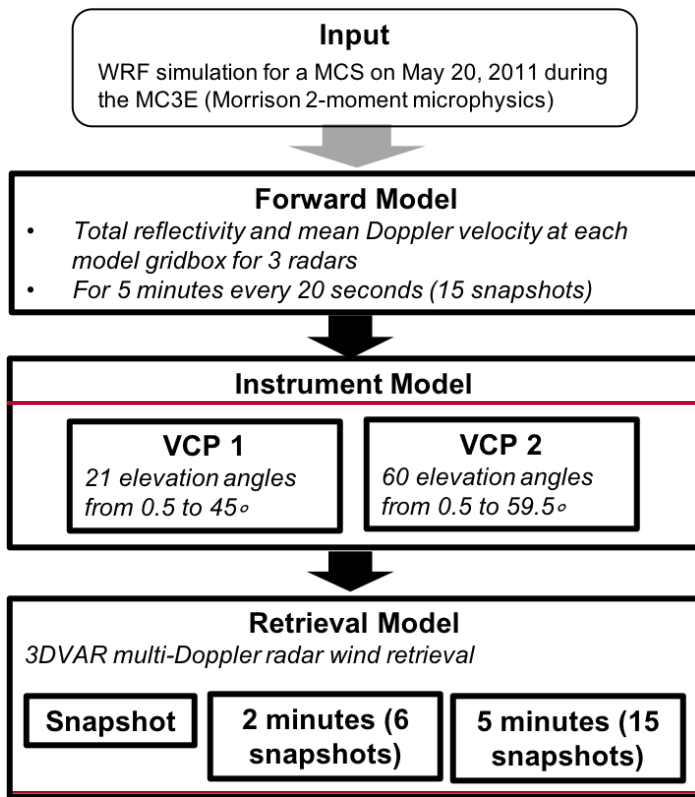
855 **Figure 7: Investigation of errors of cloud fraction profiles (CFPs) from profiling measurements. CFPs from single sites**
 are estimated by integrating over time, and then they are averaged over site. Shown are domain-averaged cloud fraction
 profiles (CFPs) from (a) WRF-simulated cloud water mixing ratio and (b) the simulated ARSCL product for a shallow
 convection case on June 11, 2016. Colors in (a) and (b) represent different integration time periods centered at 21:00:00
 UTC. The minimum threshold for the WRF cloud water mixing ratio is 0.01 g kg^{-1} . (c-h) CFPs from the simulated
 ARSCL with different number of observation sites N and different integration periods T . The black line in (c-h)
 860 represents the domain-averaged CFP from the WRF-simulated cloud water mixing ratio, blue lines represent CFPs
 from individual observation sites, and the red line represents the mean CFP from averaging over the individual sites.
 (i and j) Root mean square error (i) and mean absolute percentage error (j) of the simulated ARSCL CFPs as a function
 of the number of observation sites and integration period.

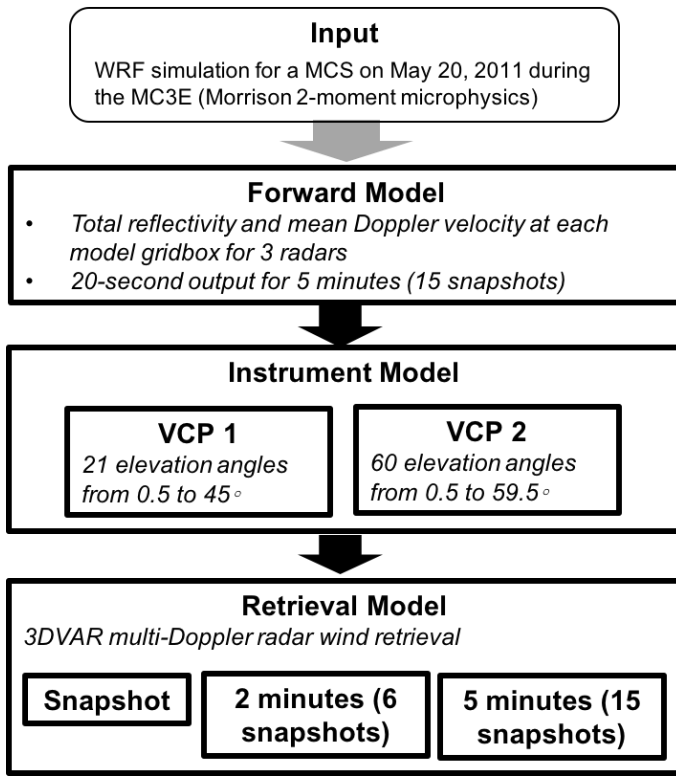


865

Figure 8: Horizontal cross sections of (a) water content simulated by WRF and (b) Ka-band (35 GHz) Z_{hh} simulated at 2.4 km above ground level for a LASSO case. In (b), it is assumed that the radar is located at $x=0$ km and the RHI is scanned along the east-west axis, and the radar sensitivity Z_{MIN} with $Z_0 = -50$ dBZ was applied. (c) Cloud fraction profiles corresponding to the 10% cumulative distribution function (CDF) isoline with changing integration time of CWRHI (hence, number of scans). (d) The root-mean-square error (RMSE) from the LES domain-averaged CFP for CDF isolines of 5% (thin solid line), 10% (thick solid line), 15% (dashed line), and 20% (dashed-dotted line) as a function of integration time. The black dashed line in (c) represents the LES domain-averaged CFP for hydrometeor mixing ratio ≥ 0.01 g kg⁻¹. (c) and (d) are adapted from Oue et al. (2016).

875





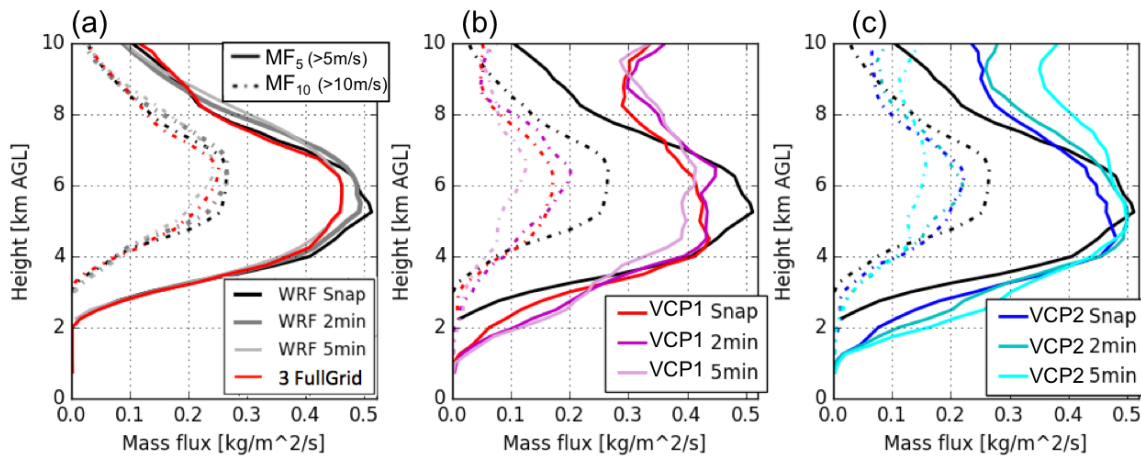
880 **Figure 9: A diagram of an Observing System Simulation Experiment study to investigate the impacts of radar volume**
 885 **coverage pattern (VCP) on a multi-Doppler radar wind retrieval.**

885

890

895

900



905 **Figure10: Vertical profiles of convective mass flux with different updraft thresholds of 5 m s^{-1} (solid lines) and 10 m s^{-1} (dashed lines). Displayed in each panel are different retrieval simulations represented by different colors. The dark gray line in (a) represents the time average of the WRF output over 2 minutes, and the light gray line in (a) represents the time average of the WRF output over 5 minutes. The profile from the WRF snapshot is displayed in each panel by a black solid line. Adapted from Oue et al. (2019a).**

910

915